Evolution of the foreland basins on either side of the Tian Shan and implications for lithospheric architecture

Chao Li, Shengli Wang, Yanjun Wang, Zhiyuan He, Chuang Sun, Hugh Sinclair, Yan Chen, Shaowen Liu, Guohui Chen, Fei Xue

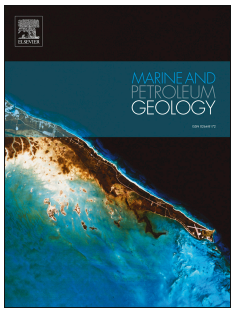

Evolution of the foreland basins on either side of the Tian Shan and implications for lithospheric architecture

Chao Li, Shengli Wang, Yanjun Wang, Zhiyuan He, Chuang Sun, Hugh Sinclair, Yan Chen, Shaowen Liu, Guohui Chen, Fei Xue

PII: S0264-8172(23)00250-7

DOI: https://doi.org/10.1016/j.marpetgeo.2023.106344

Reference: JMPG 106344

To appear in: *Marine and Petroleum Geology*

Received Date: 17 April 2023

Revised Date: 29 May 2023

Accepted Date: 30 May 2023

Please cite this article as: Li, C., Wang, S., Wang, Y., He, Z., Sun, C., Sinclair, H., Chen, Y., Liu, S., Chen, G., Xue, F., Evolution of the foreland basins on either side of the Tian Shan and implications for lithospheric architecture, *Marine and Petroleum Geology* (2023), doi: https://doi.org/10.1016/j.marpetgeo.2023.106344.

Evolution of the foreland basins on either side of the Tian Shan and implications for lithospheric architecture

Chao Li[a*], Shengli Wang[b], Yanjun Wang[c], Zhiyuan He[d], Chuang Sun[e], Hugh Sinclair[f], Yan Chen[g], Shaowen Liu[h], Guohui Chen[a], Fei Xue[a]

[a] School of Earth Sciences and Engineering, Hohai University, Nanjing 211100, China.

[b] Institute of Continental Geodynamics, School of Earth Sciences and Engineering, Nanjing University, Nanjing 210023, China.

[c] Key Laboratory of Reservoir Characterization, Research Institute of Petroleum Exploration and Development—Northwest, China National Petroleum Corporation, Lanzhou 730020, China.

[d] Laboratory for Mineralogy and Petrology, Department of Geology, Ghent University, Krijgslaan 281 S8, 9000 Ghent, Belgium.

[e] School of Geosciences and Technology, Southwest Petroleum University, Chengdu 610500, China.

[f] School of GeoSciences, University of Edinburgh, Edinburgh, UK.

[g] Univ. Orléans, CNRS, BRGM, ISTO, UMR 7327, F-45071, Orléans, France.

[h]School of Geography and Ocean Science, Nanjing University, Nanjing, China.

First author and *Corresponding author: Chao Li

Postal address: No. 8 Fochengxilu Road, Hohai University, Nanjing 211100, China

Email: lichao2019@hhu.edu.cn

Author: ShengLi Wang

Email: wangsl@nju.edu.cn

Author: Yanjun Wang

Email: wang_yj8@petrochina.com.cn

Author: Zhiyuan He

Email: Zhiyuan.He@UGent.be

Author: Chuang Sun

Email: sunchuang@mail.sysu.edu.cn

Author: Hugh Sinclair

Email: Hugh.Sinclair@ed.ac.uk

Author: Yan Chen

Email: yan.chen@univ-orleans.fr

Author: Shaowen Liu

Email: shaowliu@nju.edu.cn

Author: Guohui Chen

Email: Guohui.Chen@hhu.edu.cn

Author: Fei Xue

Email: 20200040@hhu.edu.cn

Abstract

The previous understanding of Tian Shan's lithospheric architecture can be summarized into three models: unidirectional underthrusting, bidirectional underthrusting, and mantle upwelling. These models make distinctive predictions regarding the migration and subsidence histories of the foreland basins on either side of the range. Seismic profiles crossing both foreland basins document their migration and subsidence history. We analyze a seismic profile across the Southern Junggar foreland basin (SJFB) to the north of the range, which demonstrates that the basin migrated northward at ~3.1 mm/yr during 22–16 Ma. Combining this with previously

known migration rates of the Northern Tarim foreland basin (NTFB) to the south of the range, we constrain the migration of these two foreland basins relative to their basements. We then employ an elastic plate model to simulate the subsidence profiles across these two basins at ~20 Ma, 13-16 Ma, ~5 Ma, and 0 Ma constrained by back stripping well log data and seismic records of the basin onlaps. Our modeling reveals the propagation rates of the southern and northern Tian Shan thrust wedges and the evolution of their topographic loads. Our analysis and modelling demonstrate that the NTFB has the characteristics of a retro-foreland basin, whereas the SJFB resembles a pro-foreland basin during early-middle Miocene times. This suggests that the Tian Shan's growth during this period was dominated by underthrusting of the Junggar lithosphere. Furthermore, our analysis and modelling reveal a convergent pattern between the Tarim lithosphere and the Tian Shan changed from lithospheric indentation to lithospheric subduction after the middle Miocene, as the plate setting of the NTFB and SJFB changed. The Tian Shan had begun to uplift before the middle Miocene, with the orogen's height reaching half of its present elevation before the late Miocene.

Keywords: Tian Shan, Foreland basin, Subsidence modelling, Seismic profilling, Lithospheric architecture

1 Introduction

The Asian continent underwent significant intra-continental deformation in the late Cenozoic as a result of convergence between the Indian and Asian continents, including the modern Tian Shan (Fig. 1). Although this understanding is widely accepted, there is still a debate over the intra-continental Tian Shan orogen's deep architecture (e.g. Makeyeva et al., 1992; Zhao et al., 2003; Lei and Zhao, 2007; Zhang et al., 2020; Table S1 in the supplementary material). As the largest intra-continental orogenic belt on Earth, the modern Tian Shan is a doubly vergent thrust

belt formed by the rejuvenation of the Paleozoic collisional orogenic belt triggered by the ongoing India-Eurasia collision (Molnar and Tapponnier, 1975; Windley et al., 1990; Hendrix et al., 1992; Yin et al., 1998; Dumitru et al., 2001). The understanding of the deep lithospheric architecture of the orogeny, based on geophysical investigations (Table S1), can be summarized in terms of three models (Fig. 2): (1) The unidirectional underthrusting of the Tarim lithosphere beneath the Tian Shan (Zhao et al., 2003; Steffen et al., 2011; Gilligan et al., 2014); (2) the bidirectional underthrusting of the Tarim and Junggar lithospheres (Li et al., 2016a; Lü et al., 2019); and (3) mantle upwelling caused by small-scale mantle convection in the upper mantle or the delamination of the thickened lithosphere (Roecker et al., 1993; Lei and Zhao, 2007; Li et al., 2009). The topographic uplift of the modern Tian Shan induced flexural subsidence in the Northern Tarim and the Southern Junggar blocks, forming a typical intra-continental orogenic belt-foreland basin system (Lu et al., 1994; Jia et al., 1997; Wang et al., 2001a; Qi et al., 2013). The sedimentary infill of the Northern Tarim foreland basin (NTFB) and the Southern Junggar foreland basin (SJFB) can be utilized as sources of insights into crustal shortening and topographic growth of the Tian Shan (Wang et al., 2013; Li et al., 2019; 2020; 2022a). The three models of the Tian Shan lithospheric architecture make distinctive predictions for the migration and tectonic subsidence of the foreland basin systems according to the foreland basin-mountain building theories (Johnson and Beaumont 1995; Naylor and Sinclair, 2008) (Fig. 2).

Although geophysical exploration provides a possible current lithospheric architecture of the Tian Shan, the orogen's inferred geodynamic evolution from the modern lithospheric architecture can be tested using multiple disciplines. The middle and eastern segments of the Tian Shan lack exposures of late Cenozoic synorogenic magmatic rocks (Charvet et al., 2011).The Tian Shan also lacks petrological and geochemical evidence reflecting subduction polarity of the Cenozoic

Tarim and Junggar lithospheres and the orogeny's geodynamic pattern, such as records of the residual oceanic fore-arc basins, because the orogen did not undergo a transition from oceanic-continental subduction to continental collision during the Meso-Cenozoic period (Jolivet et al., 2010; Jepson et al., 2018; Morin et al., 2019). Furthermore, Cenozoic sedimentary infill composition, provenance, and deformation styles of the shortening structure in the NTFB and SJFB are very similar (Lu et al., 1994; Li et al., 2004; Bian et al., 2010).

In the last 40 years, geologists have extensively studied the sedimentary sequences and subsidence history in foreland basins (e.g., Lyon-Caen and Molnar, 1985; Homewood et al., 1986; Johnson and Beaumont, 1995; Simoes and Avouac, 2006), and they have discovered that in orogenic belt-foreland basin systems, pro-foreland basins over underthrust lithosphere and retro-foreland basins over overriding plates contrast markedly in terms of their stratigraphic architecture, migration and subsidence histories (Johnson and Beaumont 1995; Naylor and Sinclair, 2008). Pro-foreland basins are characterized by: (1) Stratigraphic onlap onto the cratonic margin at a rate ($V_{O\text{-}P}$) equal to the sum of the plate convergence rate (V_C) and the propagation rate of thrust wedge ($V_{P\text{-}P}$); (2) accelerating tectonic subsidence driven primarily by the translation of the basin fills towards the mountain belt (Fig. 3). In contrast, retro-foreland basins are characterized by: (1) relatively little stratigraphic onlap driven only by the growth of the retro-wedge ($V_{O\text{-}R} = V_{P\text{-}R}$); (2) A constant tectonic subsidence rate during the growth of the thrust wedge, with zero tectonic subsidence during the steady-state phase (Fig. 3). Hence, we can test the lithosphere's subduction polarity and convergence rate by interpreting the basin fill architecture and subsidence (e.g., Lyon-Caen and Molnar, 1985; Simoes and Avouac, 2006; Sinclair and Naylor, 2012). According to Tian Shan's unidirectional underthrusting model, the foreland basin on one side of the range should be characteristic of a pro-foreland basin, while the

foreland basin on the counterpart should conform to the characteristics of a retro-foreland basin. The bidirectional underthrusting model, however, predicts that the foreland basins on both sides of the range could be characteristic of the plate setting of a pro-foreland basin. Finally, the mantle upwelling model predicts that the subsidence process of the foreland basins on both sides was decoupled from the topographic evolution of the Tian Shan (Fig. 2), and a positive dynamic topography should be recognized in the range. However, the subsidence process and sedimentary successions in the NTFB and SJFB, as typical foreland basins, are coupled with the growth history of the Tian Shan (Lu et al., 1994; Wang et al., 2013), and there is regional isostasy compensation beneath the Tian Shan according to the flexural and rheological modeling (Jiang, 2014). Therefore, the mantle upwelling model is not supported by the evolution of the NTFB and SJFB.

The NTFB and SJFB are the important petroliferous basins in western China, so numerous high-quality seismic profiles have been acquired for hydrocarbon exploration in these two basins (e.g., Jia et al., 1997; Wang et al., 2018), providing scientific insights into the migration and subsidence histories of the basins. Understanding of the geodynamic context of the foreland basins in terms of it being a retro- or pro-foreland basin also aids prediction of source rock maturation, and potentially reservoir architecture (Bourrouilh et al., 1995; Naylor and Sinclair, 2008; Allen and Allen, 2013). Magnetostratigraphic studies (e.g., Sun et al., 2004; Huang et al., 2006; Charreau et al., 2006; 2009; Lu et al., 2010; Zhang et al., 2014) provide reliable chronological constraints on the foreland strata in these basins. Li et al. (2019) constrained the relative migration rate of the forebulge of the NTFB relative to its basement by analyzing a ~353-km-long seismic profile (BB’ in Fig. 1) across the basin.

In this contribution, we use the stratigraphic geometries from a ~141-km-long seismic profile (AA' in Fig. 1) crossing the SJFB to obtain the northward migration rate of the basin to its basement and decipher its stratal architecture. The relative migration process of the foreland basins on either side of the Tian Shan was constrained by combining the migration rates of the NTFB and SJFB. Using back stripping based on the sedimentary sequences imaged by the two seismic profiles, we further obtain the tectonic subsidence profiles across the two foreland basins in the late Cenozoic times. Finally, we use a numerical elastic model to simulate and constrain the controls on these subsidence profiles. The propagation rates of the southern and northern Tian Shan wedges, as well as the evolution of their topographic loads in the late Cenozoic are revealed by our modelling. The comparison between the NTFB and SJFB migration and subsidence characters reveals their plate settings, and suggests a possible switch of subduction polarity of the Tarim and Junggar lithospheres beneath the Tian Shan's middle segment in the late Cenozoic.

2 Geological backgrounds

The ancestral Tian Shan orogen formed during the Paleozoic through the accretion of several island arcs and collision of continental blocks (Burtman, 1975; Windley et al., 1990; Xiao et al., 2013), with large-scale dextral strike-slip occurring in the late Carboniferous–Permian (Bazhenov et al., 1999; Laurent-Charvet et al., 2003; Wang et al., 2007; He et al., 2021a). In the Mesozoic, the Tian Shan was reactivated in response to a series of Cimmerian collisions (e.g., the collisions of Qiangtang, Lhasa, and Karakorum blocks with Eurasia) occurring along the southern Eurasia margin (e.g., Jolivet et al., 2010; Jepson et al., 2018; Morin et al., 2019). In the late Cenozoic, the Tian Shan rejuvenated as an intra-continental orogen with high topography, caused by the far-field effect of the ongoing India-Eurasia collision (Molnar and Tapponnier,

1975; Yin et al., 1998; Dumitru et al., 2001; De Grave et al., 2007). The Tian Shan uplifts significantly in the late Cenozoic attested by low-temperature thermochronology (e.g., Hendrix et al., 1992; Dumitru et al., 2001; Sobel et al., 2006; Yu et al., 2014; Chang et al., 2017a; Wang et al., 2023). The shortening structures within the folding and thrusting belts on the north and south piedmonts of the Tian Shan's middle segment (Fig. 1) reflect the late Cenozoic horizontal convergence between the Tarim and Junggar blocks, and that the Tian Shan underwent doubly vergent thrusting over the Tarim and Junggar lithospheres (e.g., Lu et al., 1994; Deng et al., 1999; Hubert-Ferrari et al., 2007; Lu et al., 2010; Wang et al., 2011; Li et al., 2012). Geophysical surveys indicate that the Tarim lithosphere dips to the north beneath the middle segment of the Tian Shan (e.g., Zhao et al., 2003; Lü et al., 2019) and even subducts to mantle depths (Sun et al., 2022b), and they attest that the underthrusting of the Tarim lithosphere produced the uplift of the range. GPS measurements and seismicity also indicate present-day growth of this orogen and an NNW-trending convergence between the Tarim and Junggar blocks (Fig. 1) (Zubovich et al., 2010; Shen and Wang, 2020). The contrast between the Quaternary shortening rate and the denudation rate in the eastern segment of the Tian Shan shows that crustal thickening outpaced denudation and sediment outflux by a factor of ~10, indicating that the range remains in a transient state of topographic growth (Charreau et al., 2023). Numerous intermontane basins were created by a post-orogenic phase of transtensive deformation during the Permian to Late Triassic (Jolivet et al., 2010). These basins are still partially preserved from Late Triassic to present, which caused a relatively low elevation in the center of the modern Tian Shan (Fig. 1) (Charreau et al., 2017).

The upliftment of modern Tian Shan above the Paleozoic and Mesozoic strata caused flexural subsidence of the NTFB and SJFB (Fig. 1; Yang and Liu, 2002) and formed the

Cenozoic foreland basin system (Lu et al., 1994; Jia et al., 1997; Wang et al., 2001a; Qi et al., 2013; Li et al., 2016b). The NTFB in Tian Shan's south piedmont has a maximum thickness of ~7 km of Cenozoic foreland strata, while the SJFB has a maximum thickness of ~5 km (Fig. 1)(Li et al., 1996; Wang et al., 2013; Li et al., 2019; 2022b).

The Cenozoic sedimentary sequences in the NTFB include the Kumugeliemu, Suweiyi, Jidike, Kangcun, Kuqa, and Xiyu Formations in ascending order from older to younger (Zhang et al., 2004). Li et al. (2019) correlated the seismic reflectors in our profile across the basin with the magnetostratigraphic studies in the southern flank of the Tian Shan (Huang et al., 2006; Charreau et al., 2009; Zhang et al., 2014) and dated the bottom of the Jidike, Kangcun, Kuqa, and Xiyu Formations as ~26.3 Ma, ~13.4 Ma, ~5.3 Ma, and ~1.7 Ma, respectively (Fig. 4). Cenozoic strata in the SJFB comprise the Ziniquanzi, Anjihaihe, Shawan, Taxihe, Dushanzi, and Xiyu Formations in an ascending order (BGMRX, 1993). The bottoms of the Shawan, Taxihe, Dushanzi, and Xiyu Formations in our seismic profile across the basin were dated at ~23.6 Ma, ~20.1 Ma, ~16 Ma, and ~4.7 Ma, respectively, by correlating the seismic reflectors with the magnetostratigraphic results in the northern Tian Shan (Fig. 4) (Charreau et al., 2005; Charreau et al., 2009; Lu et al., 2010; Wang et al., 2013).

3 Data

The basic data for reconstructing the migration and subsidence history in the SJFB and NTFB were derived from a ~141 km-long and 4-s-deep N-S trending seismic profile AA′ across the SJFB and a ~353 km-long and 6-s-deep seismic profile BB′ across the NTFB extending from the center of the Tarim basin to the Kuqa city (Figs. 1 and 5). The dominant frequency of the seismic data is 28 Hz, and theoretical vertical seismic resolution or one-quarter wavelength for the 28 Hz wavelet is ~18 ms (<45 m) in travel time. These profiles are parallel to the direction of

the convergence between the Tarim and Junggar blocks indicated by GPS measurements (Wang and Shen, 2020; Wu et al., 2023). Based on well logging data near this profile, we converted the two seismic time profiles into depth profiles. Considering the bending nature of the seismic profile BB′, we projected it onto a straight-line transverse to the NTFB axis so that it could be used in our 2-D elastic plate subsidence model (Figs. 1 and 5).

The stratigraphic thicknesses used in back stripping calculations are derived from the converted depth profiles of seismic profiles AA′ and BB′ (Fig. 5b-d). The decompaction parameters used in the calculation are derived from Sclater and Christie (1980) (Table 1); while the lithology, density, and top and bottom depths of each layer are obtained from profiles and well logging data. We ignored eustatic sea-level changes because the epicontinental sea only reached the western margins of the Tarim and Junggar basins in the Paleogene, and eventually became isolated from the basins in the late Eocene (Bosboom et al., 2011; Li et al., 2018). The paleobathymetry is estimated using sedimentary environment analyses of each stratigraphic unit (e.g., Guo et al., 2002; Li et al., 2004; Shao et al., 2006; Bian et al., 2010; Yang et al., 2013), and incorporates broad error bars.

The main parameters of the elastic plate model, for modelling the evolution of subsidence in the NTFB and SJFB and the growth of the Tian Shan, include the density, width, surface slope angle α, basal decollement dip angle β of the southern and northern Tian Shan thrust wedges, as well as the effective elastic thickness *Te*, Poisson's ratio *v*, Young's modulus *E* of the Tarim and Junggar lithospheres, and density of the asthenosphere mantle ρ_m (Fig. 6). The α and the present-day width of the thrust wedges are obtained from an 80 km wide swath topographic profile across the middle segment of the Tian Shan (Fig. 1c), where the α of the northern Tian Shan wedge is ~2.4° and that of the southern Tian Shan is ~1.5°. In our model, the parameters, *v*

(0.25), E (5×10^{10} Pa), ρ_m (3300 kg m^{-3}), and gravity acceleration g (9.81 m s^{-2}) were set to standard values (Aitken, 2011). Since the southern and northern Tian Shan thrust wedges are mainly composed of Proterozoic–Paleozoic magmatic or metamorphic rocks (Xiao et al., 2013), the average density of the thrust wedges in our model is set to the standard value for ancient thrust wedge density (2800 kg/m^3) (Saura et al., 2015).

The wide-angle seismic reflection/refraction profiling across the Tian Shan from Karamay to Kuqa reveals the complex decoupling architecture of the lower and middle crust and lithospheric mantle of the Tarim and Junggar blocks beneath the junctions of the two basins and the Tian Shan, which alters the crustal thickness of the Tarim and Junggar blocks (Zhao et al., 2003). Therefore, although the shear wave velocity model of the crust and upper mantle of the Tian Shan shows the dip angle of the Moho surface beneath the basin-mountain junctions (Lü et al., 2019), the dip angle of the Moho cannot constrain the β of the southern and northern Tian Shan wedges. We determined the values of β of the thrust wedges in our model according to the geometry of the wedge coupled with the present-day tectonic subsidence profiles across the basins in modelling results.

4 Methods

4.1 Quantifying the migration of the Southern Junggar foreland basin

We tracked all the seismic reflectors in profile AA′ and identified northward onlap points of the foreland sequence in the SJFB based on the northern termination sites of the reflectors. The termination of a seismic reflector to the foreland (stratal onlaps in the foreland basin) represents the distal end of deposition at that time. Generally, the thinnest sedimentary sequences or no sediments occur in the forebulge of a foreland basin system, and thicken to the foredeep (DeCelles & Giles, 1996). Accordingly, the envelope line of the distribution area of

forelandward reflector terminations denotes the boundary between the foredeep and the forebulge (Li et al., 2019; Wang et al., 2020). Thus, the migration of the boundary relative to the underlying plate can reflect that of a foreland basin (Fig. 6). Wang et al. (2013) divided the sedimentary sequences in the SJFB into four tectonostratigraphic units according to the unconformities between them. The upper-most unit is the Miocene-Quaternary foreland basin unit which is associated with the late Cenozoic uplift of the Tian Shan. We tracked all the seismic reflectors and determined the positions of their terminations in the Miocene-Quaternary foreland basin unit imaged by profile AA′. The envelope line of the terminations of reflectors in this foreland unit represents the trace of the southward migration of the forebulge of the SJFB.

Recent magnetostratigraphic studies of the Cenozoic strata in the northern Tian Shan provide a chronostratigraphic framework (Fig. 4). The detailed ages of the Cenozoic strata were correlated with profile AA′ and extrapolated across the SJFB through a crossing seismic profile (Wang et al., 2013). The ages of the seismic reflectors in the foreland basin were interpolated by an assumption that the sedimentation rate between any two reflectors is constant. According to the ages of seismic reflectors and distances between reflectors' terminations and the northern Tian Shan wedge, the linear-regression of the onlap points on the envelope line yields a migration rate of the forebulge in the SJFB relative to its basement.

4.2 Modelling subsidence evolution of the NTFB and SJFB

4.2.1 Back stripping

To model subsidence in the NTFB and SJFB, we applied a 2-D elastic rheology plate model. Most flexural basins' observed basement subsidence profiles can be roughly predicted by the 2-D elastic plate model in first-order (e.g., Yang and Liu, 2002; Saura et al., 2015). The

observed tectonic subsidence profiles across the basins from back stripping are the constraints for modelling the evolution of subsidence of the NTFB and SJFB.

We divided the Cenozoic strata in the foredeep of the NTFB into three units using the continuous seismic reflectors that correspond to the bottoms of the Kangcun (~13.4 Ma) and Kuqa Formations (~5.3 Ma) in profile BB' (Fig. 5). Back stripping these units, we obtained the observed tectonic subsidence profiles across the NTFB at ~13 Ma, ~5 Ma, and the present. The Cenozoic strata in the SJFB are divided into four units using the continuous reflectors that correspond to the bottoms of the Taxihe (~20.1 Ma), Dushanzi (~16.0 Ma) and Xiyu Formations (~4.7 Ma) in profile AA' (Fig. 5). Back stripping these units yielded observed tectonic subsidence profiles across the SJFB at ~20 Ma, ~16 Ma, ~5 Ma, and the present. The procedure of back stripping includes decompaction, paleobathymetric correction, and flexural isostatic stripping for calculating the tectonic subsidence (Allen and Allen, 2013). This methodology requires some basic information including the lithology, top and bottom depths, age, decompaction parameters (Table 1) and the paleo-water depth of each stratigraphic unit.

According to Li et al. (2020), the sediment drape created by the Tarim Basin's base level rise since the Oligocene was not related to the tectonic load of the Tian Shan. Hence, we separated the sediment drape from the tectonic subsidence before the flexural back stripping. The calculation by Li et al. (2020) was used to determine the thickness of the sediment drape in this procedure.

4.2.2 Numerical model

The tectonic load of the thrust wedge is imposed onto a semi-infinite elastic plate floating on the asthenosphere in the model. We employ the finite difference solution for the flexure equation based on a Python script called ‘Gflex’ (Wickert, 2016). Given that the critical angle of thrust

297 wedges tends to remain stable over millions of years (Davis et al., 1983), and no research has
298 documented changes in the critical angle of the Tian Shan, we reduced the tectonic loads of the
299 northern and southern Tian Shan thrust wedges to a triangular wedge imposed on the end of the
300 plate with a fixed critical wedge angle ($\alpha+\beta$ in Fig. 6).

301 Main parameters in the elastic plate model contain the Te, E, ν, ρ_c, ρ_m, g of the Tarim and
302 Junggar blocks, and the wedge angle (α, β), density (ρ_o) and width (W) of the thrust wedges of
303 the Tian Shan. For the modern NTFB and SJFB (0 Ma), the Te and β are only two unknown
304 variables in our modelling while the other parameters are known. The optimal values for these
305 two parameters are determined by minimizing the misfit between the observed and modelled
306 subsidence profiles across the Tarim Basin. There are certain trade-offs between the Te and β.
307 We apply the downhill simplex algorithm (Wright, 1996) to determine the best combination of
308 these two variables, and utilize Python's scipy fmin function to implement the downhill simplex
309 algorithm. We model the best combination of the Te of the modern Tarim and Junggar blocks
310 and the β of the modern thrust wedges using the trial-error method carrying out through a Python
311 program based on the 'Gflex' and the 'fmin.' For the historic NTFB and SJFB (~20 Ma, ~13–16
312 Ma, ~5 Ma), the historic Te and W are treated as variables in our modelling. We model the best
313 combination of the historic Te of the Tarim and Junggar blocks and the historic W of the thrust
314 wedges also using the trial-error method as described above.

315 The optimal values of W in the modelling results at ~20 Ma, ~13–16 Ma, ~5 Ma, and the
316 present-day indicate the variations in the W of the southern and northern Tian Shan thrust
317 wedges. Based on the variations in the W (P in Fig. 6), we calculated the propagation rates of the
318 southern and northern Tian Shan wedges (V_P in Fig. 3) in the direction perpendicular to the trend
319 of the range.

We also took into account how the modelling outcomes could be affected by the horizontal convergence distance between the mountain wedge and the foreland basin basement (*C* in Fig. 6). Taking the SJFB as an example, we use the first end-member model with a minimum (zero) horizontal convergence distance ($C = 0$), which represents a retro-foreland basin system, to model the observed subsidence profiles at 0 Ma, ~4.7 Ma, ~16.0 Ma, and ~20.1 Ma. In this case, the distance between the tectonic subsidence profiles from profile AA' at each time point and the backstop of the northern Tian Shan wedge, the horizontal axis zero point, is the same. In other words, the observed basin subsidence profiles at ~4.7 Ma, ~16.0 Ma, and ~20.1 Ma are at the theoretical minimum distance from the thrust wedge. Based on the flexural isostasy, the required tectonic load to cause the same amount of subsidence is proportional to the distance between the load and the subsidence point (Turcotte and Schubert, 2002). The closer the distance, the lesser the tectonic load required to induce the same amount of subsidence. Therefore, the predicted tectonic loads of the northern Tian Shan wedges at ~4.7 Ma, ~16.0 Ma, and ~20.1 Ma in this end-member model are at the theoretical minimum, representing the minimum of their width (*W*) and the maximum of the propagation distance of the wedge (*P*) (Figs. 3 and 6).

For the second end-member model, we model the observed subsidence profiles at 0 Ma, ~4.7 Ma, ~16.0 Ma, and ~20.1 Ma by using the maximum horizontal convergence distance that is equal to the migration distance of the foreland basin ($C = O$ in Fig. 6), which represents a pro-foreland basin-thrust wedge system in a steady state (Naylor and Sinclair, 2008). In this case, the observed tectonic subsidence profiles at ~4.7 Ma, ~16.0 Ma, and ~20.1 Ma were restored to a pre-convergence position at a distance of the *C* from the top of the modern thrust wedge top. Based on the elastic flexure, the predicted tectonic loads of the northern Tian Shan wedges at ~4.7 Ma, ~16.0 Ma, and ~20.1 Ma in this end-member model are at the theoretical maximum

because we used the maximum horizontal convergence distance, reflecting the maximum of their width (W) and the minimum propagation distance of the wedge (P). Hence, the maximum and minimum values of the propagation distance of the southern and northern Tian Shan wedges (P), as well as the range of their propagation rate V_P, were determined by our modelling using two end members.

The results derived from the two end-member models constrain the ranges of the P and C in the NTFB and SJFB systems. Combining the stratigraphic age framework, we calculate the ranges of the propagation (V_P) and convergence (V_C) rates of the southern and northern Tian Shan thrust wedges.

5 Analyzing migration rate of the foreland basins

The profile AA′ depicts the structures and strata thickness variations in the SJFB (Fig. 7). The fault-related folds of the northern Tian Shan fold-thrust belt form the southern part of the profile, with the foredeep to the north. There is a thrust in the fold-thrust belt that occurs within a Jurassic coal bed and has two arrays of growth anticlines in its hanging wall (Fig. 7; Wang et al., 2013). The foredeep sedimentary layers comprise late Paleozoic-Cenozoic strata. The Shanwan, Taxihe, Dushanzi and Xiyu Formations in the upper part of the profile constitute the Miocene-Quaternary foreland sedimentary layer, which is associated with the growth of the Tian Shan (Fig. 7; Wang et al., 2013).

We tracked 64 reflectors in the foreland sedimentary layer, which were named R1 through R64 in an ascending order (Figs. 7 and S1; Table S2 in the Supplementary material). Reflectors R1 to R64 extend or terminate northwards within the seismic profile. There are 17, 11, 21, and 15 reflectors in the Shawan, Taxihe, Dushanzi and Xiyu Formations, respectively. Reflectors R1–R30 in the Shawan, Taxihe Formations, and the lower part of the Dushanzi Formation are

366 well imaged and may thus be tracked credibly (Fig. 7). These reflectors are characterized by
367 sequential northward onlaps. We determined the positions of their northward terminations that
368 reflect the northward migration of onlapping points in these formations (Table S2). From R1 to
369 R29, the termination points expand northwards for ~93 km. The profile does not image R31–R64
370 in the upper Dushanzi Formation and the Xiyu Formation completely, therefore their seismic
371 nature and terminations cannot be determined. As a result, the migration of the onlap sites in the
372 Dushanzi and Xiyu Formations was not calculated.

373 Although terminations of seismic reflectors go back and forth with time (Figs. 7 and S1),
374 they migrate to the foreland overall. As described in section 4.1, the envelope of the distribution
375 area of forelandward reflector terminations indicates the migration of the foreland basin (Fig. 6).
376 To quantify the migration of the SJFB, we plotted the ages of strata represented by reflectors
377 versus the distances between reflector terminations and the northern Tian Shan wedge (the
378 boundary between the fold-thrust belt and the foredeep in Fig. 7). According to the ages of
379 seismic reflectors and their termination positions, the linear-regression analysis suggests that the
380 northward onlaps in the foreland sequence of the SJFB migrated at a rate of 44.6 ± 3.1 mm/yr
381 along 85°E from ~23 Ma to ~22 Ma (R1–R9), and migrated at a rate of 3.1 ± 0.2 mm/yr from
382 ~22 to ~16 Ma (R9–29) (see details of onlap rate uncertainty calculation in the Supporting
383 Information S1) (Fig. 8). The migration rate of the onlap points from ~23 to ~22 Ma even
384 outpaces the convergence rate (~40 mm/yr) between the Indian and Eurasian plates during the
385 same period based on paleomagnetic records (Guillot et al., 2003; Copley et al., 2010). Hence,
386 the onlaps from ~23 to ~22 Ma (R1–R9) may reflect the initial filling process of the foreland
387 basin rather than the forebulge's migration within the basin driven by the convergence between
388 the Junggar block and the northern Tian Shan. The migration rate of the northward onlaps in

foreland sequences from ~22 to ~16 Ma should reflect the northward migration rate V_O (Fig. 3) of the SJFB relative to the wedge top of the northern Tian Shan (Wang et al., 2013; Li et al., 2022).

Li et al. (2019) applied the method described above to identify the onlap points in the Cenozoic foreland basin unit imaged by profile BB′ across the NTFB and calculated the migration rates of the foreland basin (*Vo* in Fig. 3) based on magnetostratigraphic constraints. The forebulge of the NTFB migrated southward at a rate of 1.6 ± 0.1 mm/yr between ~26 and ~12 Ma, and at a rate of 14.6 ± 0.1 mm/yr after ~12 Ma.

6. Modelling results

6.1 The Northern Tarim foreland basin

By back stripping the foreland strata in the profile BB′, we obtained the tectonic subsidence profiles across the NTFB at ~13.4 Ma, ~5.3 Ma, and the present day (Fig. 5). We used the first end-member model without horizontal convergence ($C = 0$) to model the observed subsidence profiles, and the results reflect the maximum value of the P of the southern Tian Shan wedge (Fig. 9a–c).

The width of the southern Tian Shan thrust wedge is a known value when modelling the observed a tectonic subsidence profile at 0 Ma, whereas its β is a variable. The swath topographic profile indicates that the width of the thrust wedge is ~92 km (Fig. 1). The modelling results demonstrate that the best fit between the observed and predicted subsidence profile is achieved with the optimal value of the *Te* of ~61 km and the β of the southern Tian Shan thrust wedge of ~7.8°.

The optimal width of the southern Tian Shan thrust wedge has increased from ~53 km to ~71 km from ~13.4 Ma to ~5.3 Ma with an average propagation rate of ~2.2 mm/yr, and increased

from ~71 km to ~92 km since ~5.3 Ma with an average propagation rate of ~4.4 mm/yr, based on modelling results of the observed subsidence profile at ~13.4 Ma and ~5.3 Ma. The modelling results also reveal that the optimal value of the *Te* of the Tarim block has gradually increased from ~58 km to ~61 km from ~13.4 Ma to the present.

Using the second end-member model with a theoretical maximum value of the horizontal convergence between the thrust wedge and basin basement, the minimum value of propagation (*P*) of the southern Tian Shan thrust wedge are predicted by modelling the observed subsidence profiles across the NTFB (Fig. 10a–c).

The same results were obtained in this modelling because the modelling parameters at 0 Ma were the same as those of the first end-member model with no horizontal convergence.

When modelling the observed subsidence profiles at ~13.4 Ma and ~5.3 Ma, the horizontal convergence distance (*C* in the model) between the Tarim block and the southern Tian Shan wedge, was set at ~137 km and ~54 km, respectively, for the profiles at ~13.4 Ma and ~5.3 Ma according to the migration distance of the NTFB (*O*), as determined by seismic profiles analysis (Li et al., 2019). To restore the observed subsidence profiles at ~13.4 Ma and ~5.3 Ma to their pre-convergence positions, they were moved southward by ~137 km and ~54 km, respectively. According to the modelling, the predicted width of the southern Tian Shan wedge has remained constant at ~92 km since ~13.4 Ma, indicating a theoretical minimum propagation rate of zero. The modelling also revealed that the optimal value of *Te* was ~90 km at ~13.4 Ma and has decreased to 61 km.

6.2 The Southern Junggar foreland basin

We obtained the tectonic subsidence profiles across the SJFB at ~20.1 Ma, ~16.0 Ma, ~4.7 Ma, and the present day by back stripping the foreland strata in the profile AA′ (Fig. 5). We used

435 the first end-member model with no horizontal convergence to model the observed subsidence
436 profiles, and the outcomes reflected the maximum value of propagation of the northern Tian
437 Shan wedge (*P*) (Fig. 9d–g).

438 When modelling the observed tectonic subsidence profile at 0 Ma, the width of the northern
439 Tian Shan wedge is a known value, while its β is variable. According to the swath topographic
440 profile, the thrust wedge is ~71 km wide (Fig. 1). The modelling results show that a *Te* of 35 km
441 and β of 7.0° for the northern Tian Shan wedge are optimal for achieving the best fit between the
442 observed and predicted subsidence profile.

443 The modelling results of the observed subsidence profiles at ~20.1 Ma, ~16.0 Ma, and ~4.7
444 Ma indicate that the width of the northern Tian Shan wedge has increased from ~42 km to ~53
445 km during 20.1–16.0 Ma with an average propagation rate of ~2.6 mm/yr, from ~53 km to ~62
446 km during 16.0–4.7 Ma with an average rate of ~0.8 mm/yr, and from ~62 km to ~71 km since
447 ~4.7 Ma with a rate of ~1.9 mm/yr. The modelling results also show that from ~20.1 Ma to the
448 present, the optimal value of the *Te* of the Junggar block has gradually increased from ~33 km to
449 ~35 km.

450 Using the second end-member model with a theoretical maximum value of the horizontal
451 convergence between the thrust wedge and basin basement, the minimum value of propagation
452 (*P*) of the northern Tian Shan wedge is predicted by modelling the observed subsidence profiles
453 across the SJFB, (Fig. 10d–g).

454 The modelling conditions at present were identical to those of the first end-member model
455 with no horizontal convergence, yielding the same results.

456 The value of the convergence distance (*C*) was set at ~19 km, ~7 km, and ~3 km when
457 modelling the observed subsidence profiles at ~20.1 Ma, ~16.0 Ma, and ~4.7 Ma, respectively,

according to the migration distance of the SJFB obtained by analyzing seismic profiles (Li et al., 2022). The observed subsidence profiles at ~20.1 Ma, ~16.0 Ma and ~4.7 Ma were moved northward by ~19 km, ~7 km and ~3 km, respectively, to restore them to their pre-convergence positions. According to the modelling, the northern Tian Shan wedge's predicted width increased from ~49 km to ~58 km during 20.1–16.0 Ma with an average propagation rate of ~2.2 mm/yr, from ~58 km to ~66 km during 16.0–4.7 Ma with an average rate of ~0.7 mm/yr, and from ~66 km to ~71 km from ~4.7 Ma to the present with an average rate of ~1.1 mm/yr. The modelling also showed that the *Te* was at its ideal value of ~42 km at ~20.1 Ma and then reduced to the present-day ~35 km.

6.3 The convergence rate

The range of the horizontal convergence rates between the Tarim block and the Tian Shan are constrained according to the propagation rates of the southern Tian Shan thrust wedge (derived from the modelling results) and the range of the onlap rates of the foreland sequence within the NTFB (Fig. 11 and Table 2). The modelling results show a range of the propagation rates of 0–2.2 mm/yr for the southern Tian Shan thrust wedge during 13.4–12.0 Ma, with a maximum value exceeding the observed onlap rate of foreland sequences (~1.6 mm/yr) during the same time period. This yields a horizontal convergence rate range of 0–1.6 mm/yr. From ~12.0 Ma to ~5.3 Ma, the range of predicted propagation rates of the wedge was 0–2.2 mm/yr, and the onlap rate of the foreland sequence strata was ~14.6 mm/yr (Li et al., 2019), resulting in a horizontal convergence rate range of 12.4–14.6 mm/yr. From ~5.3 Ma to ~1.7 Ma, the range of predicted propagation rates of the wedge was 0–4.38 mm/yr, the onlap rate was ~14.6 mm/yr, leading to a horizontal convergence rate range of 10.2–14.6 mm/yr.

Based on the predicted propagation rates of the northern Tian Shan wedge and the onlap rates of the foreland sequences in the SJFB, we calculated the range of the horizontal convergence rates between the Junggar block and the northern Tian Shan (Fig. 11). From ~20.1 Ma to ~16.0 Ma, the range of horizontal convergence rates was 0.5–0.9 mm/yr according to the onlap rate of ~3.1 mm/yr and the range of predicted propagation rate of the northern Tian Shan of 2.2–2.6 mm/yr. From ~16.0 Ma to ~4.7 Ma, the range of the predicted propagation rates was 0.7–0.8 mm/yr, but the onlap rates of the foreland sequence in the SJFB are unknown during this period because the Dushanzi and Xiyu Formations are not entirely imaged in the profile AA′. Another seismic profile located ~40 km west of profile AA' shows that the conglomerate-sandstone transition in the basin-fill of the SJFB migrated northward at a rate of 0.4 ± 0.1 mm/yr from ~23 Ma to ~6 Ma along the longitude of 84°E. The forelandward migration rate of the conglomerate-sandstone transition in foreland basins is thought to be similar to the forelandward onlap rate of the basins (e.g., Burbank et al., 1988; Schlunegger & Norton, 2015; Dingle et al., 2016). The migration rate (0.4 ± 0.1 mm/yr) of the conglomerate-sandstone transition in the SJFB is lower than the predicted propagation rate (0.7–0.8 mm/yr) of the northern Tian Shan wedge from ~16.0 Ma to ~4.7 Ma. Considering that the lateral variation within 40 km has little effect on migration rate magnitude, the horizontal convergence rate between the Junggar block and the northern Tian Shan is close to zero during this period.

6.4 Tectonic subsidence rate

We obtained the changes in the tectonic subsidence rates in the NTFB and SJFB since the Neogene, corrected for sediment loading by back stripping for the seven wells in these two basins. Wells 4, 5, 6, and 7 are located in the NTFB, with Well 4 being in the center of the foredeep and Well 7 being in the proximal foredeep (Figs. 1 and 4).

The tectonic subsidence curves from these four wells show the maximum tectonic subsidence in the NTFB at ~3.5 km, and the convex-upward patterns of accelerating subsidence rates from ~26 Ma to the present (Table 3; Fig. 12), in accordance with the tectonic subsidence trend in typical pro-foreland basins (DeCelles and Giles, 1996; Naylor and Sinclair, 2008; Sinclair and Naylor, 2012). Wells 8, 9, and 10 are located in the SJFB, with Well 10 being in the distal foredeep and Well 8 being in the proximal foredeep. The subsidence curves from these three wells show that the maximum tectonic subsidence in the basin is ~1.2 km, with a tectonic subsidence rate faster than that of the NTFB from ~20 Ma to ~16 Ma. The subsidence rate rapidly decreased from ~12 Ma to ~5 Ma and was lower than that of the NTFB. Since ~5 Ma, the tectonic subsidence of these three wells has accelerated again, but the subsidence rate was still lower than that of the NTFB. These tectonic subsidence curves show a tectonic subsidence trend non-conforming to the characters of pro- or retro-foreland basins (Table 3; Fig. 12).

7 Discussion

The forelandward migration rates and subsidence history of the NTFB and SJFB are derived from the seismic profiles across these basins. Based on the migration rates and observed subsidence profiles, we used an elastic numerical model to describe the evolution of tectonic subsidence in the foreland basins combined with the formation of the southern and northern Tian Shan wedges. The modelling results reveal the evolution of the tectonic load and propagation rates of the southern and northern Tian Shan.

7.1 Deep lithospheric architecture beneath the Tian Shan unveiled by its bilateral foreland basins

The relationship between the foreland sequences onlap rates in the NTFB and SJFB and the propagation rates of the southern and northern Tian Shan thrust wedges show the plate setting

characteristics of these two basins since ~20 Ma according to the foreland basin-thrust wedge theories (Johnson and Beaumont 1995; Sinclair, 2005; Naylor and Sinclair, 2008). The data suggests a two-stage evolution of the deep lithospheric architecture of the middle segment of the Tian Shan (Fig. 13).

From the early to middle Miocene, the Tian Shan region experienced the first stage of lithospheric evolution. On the northern side of the Tian Shan, the onlap rate of the foreland sequence in the SJFB depicted by profile AA′, ~3.1 mm/yr ($V_{O\text{-}J}$ in Fig. 13a) during ~20–16 Ma, was larger than the predicted propagation rate of the northern Tian Shan wedge, 2.2–2.6 mm/yr ($V_{P\text{-}J}$ in Fig. 13a) (Fig. 11 and Table 2). This is consistent with the characteristic of a pro-foreland basin where stratal onlaps onto the basin basement toward the foreland have a rate higher than the propagation rate of the coupled thrust wedge (Fig. 3) (Johnson and Beaumont 1995; Naylor and Sinclair, 2008). Hence, the SJFB is characteristic of the plate setting of a pro-foreland basin. On the southern side of the Tian Shan, the time equivalent onlap rate of the foreland sequence in the NTFB is ~1.6 mm/yr ($V_{O\text{-}T}$ in Fig. 13a), which is only approximately half that of the SJFB. Low-temperature thermochronological studies and balanced section analyses reveal that the southern Tian Shan thrust wedge experienced at least one phase of rapid uplift, exhumation and shortening event during 20–16 Ma (Hubert-Ferrari et al., 2007; Yu et al., 2014; Chang et al., 2017a). This indicates that the southern Tian Shan wedge began to propagate during this stage (Dumitru et al., 2001; Du et al., 2007). Its propagation rate ($V_{P\text{-}T}$ in Fig. 13a) could be on the same order of magnitude as that of the northern Tian Shan wedge (2.2–2.6 mm/yr), as indicated by the estimate of balanced sections in the southern Tian Shan fold-thrust belt (Li et al., 2023), and the sandbox modelling (Sun et al., 2022a) and numerical modelling (Naylor and Sinclair, 2007) of doubly vergent orogeny. Therefore, the stratigraphic onlap in the

NTFB at a low rate of, ~1.6 mm/yr ($V_{O\text{-}T}$ in Fig. 13a), should be dominantly induced by the southward propagation of the southern Tian Shan wedge ($V_{P\text{-}T}$ in Fig. 13a) in this period. This reflects that the NTFB is characteristic of the plate setting of a retro-foreland basin. In addition, the tectonic subsidence rate of the SJFB during this stage is faster than that of the NTFB (Fig. 12), confirming the prediction that pro-foreland basins have rapid and accelerating subsidence, whereas retro-foreland basins have slowing subsidence (Sinclair and Naylor, 2012). Therefore, the observation that the NTFB on southern side of the Tian Shan was characteristic of a retro-foreland basin, while the SJFB on the counterpart conformed to the characteristics of a pro-foreland basin, is consistent with the predictions of the Tian Shan's unidirectional underthrusting model (Fig. 13a). This implies that the Tarim Block beneath the retro-foreland basin likely acted as an overriding plate in this stage, while the Junggar Block beneath the pro-foreland basin as an underthrusting plate, according to the foreland basin-thrust wedge theories (Sinclair, 2005; Naylor and Sinclair, 2008; Sinclair and Naylor, 2012).

The ongoing India-Eurasia collision revitalized the Paleozoic Tian Shan orogen (Tapponnier et al., 1982; Dayem et al., 2009), meaning that the Tarim block (northward moving) was the 'active block' and the Junggar block was the 'passive block' during their convergence. Lithosphere indentation and mantle subduction are two main drivers that can create and sustain intraplate orogenesis (Ellis, 1996; Sun et al., 2022a). Given that the plate settings of the NTFB and SJFB reveal the Junggar block as the underthrusting lithosphere and the Tarim block as the overriding lithosphere during this period, we hypothesize that the Tarim block recessed into the Tian Shan, acting as an 'indenter' to generate Tian Shan uplift (Fig. 13a). This is analogous to the late Cenozoic intra-continental orogeny of the Qilian Shan on the northern margin of the Tibetan Plateau, which was driven by lithospheric indentation-mode convergence between the

572 Qaidam block and the North China craton (Zuza et al., 2016; Sun et al., 2022a). The passive
573 underthrusting of the Junggar block beneath the Tian Shan during this stage could also be the
574 reactivation of the Paleozoic southward subduction structures of the Junggar block beneath the
575 northern Tian Shan, which was inherited from the late Paleozoic collision of blocks in the region
576 (Charvet et al., 2011; Xiao et al., 2013).

577 During 16–12 Ma, the predicted propagation rate of the northern Tian Shan wedge from the
578 modelling results decreased to 0.7–0.8 mm/yr but exceeded the migration rate (0.4 ± 0.1 mm/yr)
579 of the conglomerate-sandstone transition in the basin-fill of the SJFB imaged by seismic
580 profiling, which is considered to be close to the forelandward onlap rate of the basins (e.g.,
581 Dingle et al., 2016; Li et al., 2022). This implies that the foreland onlap rate of the SJFB during
582 16–12 Ma could not have been higher than the propagation rate of the northern Tian Shan. When
583 combined with the observation that the tectonic subsidence rate in the SJFB slowed down
584 significantly between 16–12 Ma (Fig. 12), the SJFB may have become characteristic of a retro-
585 foreland basin during this period, rather than those of a pro-foreland basin (Naylor and Sinclair,
586 2008). This suggests that the underthrusting of the Junggar block may have stalled. The
587 stratigraphic onlap rate (~1.6 mm/yr) in the NTFB during 16–12 Ma, is likewise smaller than the
588 maximum predicted propagation rate of the southern Tian Shan wedge, of ~2.2 mm/yr.
589 Consequently, the NTFB is still characteristic of the plate setting of a retro-foreland basin
590 between ~16 Ma and ~12 Ma.

591 From the late Miocene until the present, the Tian Shan region experienced the second stage
592 of lithospheric evolution. During this time, the stratigraphic onlap rate in the NTFB ($V_{O\text{-}T}$ in Fig.
593 13b) of ~14.6 mm/yr substantially exceeded the predicted propagation rate of the southern Tian
594 Shan wedge of ~2.2 mm/yr from ~12 Ma to ~5 Ma, and the rate of ~4.4 mm/yr from ~5 Ma to

the present (Fig. 11; Table 2). Additionally, the tectonic subsidence of the Tarim Basin accelerated significantly during this period, exceeding the subsidence rate of the SJFB (Fig. 12; Table 3). Our findings suggest that the Tarim Basin evolved into the plate setting of a pro-foreland basin, aligning with the typical features associated with pro-foreland basins (Fig. 3). This implies that the Tarim Block formed the underthrusting lithosphere beneath the Tian Shan (Fig. 13b). The foreland onlap rate of the SJFB ($V_{O\text{-}J}$ in Fig. 13b) during this period, as revealed by the conglomerate-sandstone transition migration rate (Li et al., 2022), was still smaller than the predicted propagation rate of the northern Tian Shan wedge ($V_{P\text{-}J}$ in Fig. 13b), which ranged from 0.4–1.9 mm/yr. Also, the tectonic subsidence rate in the SJFB decreased compared to before ~16 Ma (Table 3), which is consistent with the tectonic subsidence trend in retro-foreland basins. Therefore, the SJFB was characteristic of the plate configuration of a retro-foreland basin during this period, suggesting that the Junggar block evolved into the overriding lithosphere beneath the Tian Shan.

The change like the foreland basins on both sides of the Tian Shan after the middle Miocene indicates a shift in the convergence pattern of the Tarim Block towards the Tian Shan, from lithospheric indentation to lithospheric subduction (Fig. 13). The current unidirectional underthrusting mountain-building model of the Tian Shan unveiled by the evolution of its bilateral foreland basins is consistent with the deep architecture model in which the Tarim block's lithosphere was subducted to mantle depths beneath the southern Tian Shan (Fig. 2), as revealed by ambient noise tomography (Sun et al., 2022b). It is also in agreement with the results of the wide-angle seismic reflection/refraction profiling from Karamay to Kuqa, which show that the Moho of the Tarim block dips down to the north beneath the southern Tian Shan, while there

is a continuous and flat Moho beneath the junction of the northern Tian Shan and Junggar Basin (Zhao et al., 2003; Gilligan et al., 2014).

The migration and subsidence history of the NTFB and SJFB indicate that the Tarim block indented northward into the Tian Shan during the early to middle Miocene, triggering its uplift. From the late Miocene to the present, the convergence pattern between the Tarim and Junggar blocks changed from lithospheric indentation to subduction, with the Tarim block presently subducting beneath the Tian Shan (Fig. 13b).

The tectonic regime of the Tibetan Plateau during this period may have influenced the transformation of the deep architecture of the Tian Shan in the middle to late Miocene (Dayem et al., 2009; Huangfu et al., 2021). The finite element numerical simulation reveals that the direct contact and collision between the Indian and Tarim lithospheric mantles beneath western Tibet occurred, ~30 Ma after the India-Eurasia initial collision, dominating the late Cenozoic mountain building of the Tian Shan (Huangfu et al., 2021). The direct collision facilitated the compression stress transmission over a large distance from the India plate to the Tian Shan (Calignano et al., 2015; Huangfu et al., 2021) to cause rapid uplift of the mountain range since the middle Miocene (e.g., Yu et al., 2014; Wang et al., 2023). Therefore, the increase in stress transmitted from the Tarim block to the Tian Shan could be the main driver for the change of the convergence patterns from lithosphere indentation to subduction. The restriction of the southward underthrusting of the Junggar block after the middle Miocene might be a result of the re-locking of the décollement structures between the Junggar block and the northern Tian Shan wedge, due to the increased topographic load of the latter (Burov and Toussaint, 2007). Furthermore, due to the encounter with deep high-density layers, the increasing resistance of the underthrusting Junggar lithospheric mantle may also limit subsequent underthrusting (Capitanio et al., 2010). In

addition, during the Miocene epoch, the delamination and break-off of the Indian and Asian lithospheres resulted in the outward growth of the Tibetan Plateau (Kapp & DeCelles, 2019), which involved rapid surface uplift within northern Tibet, the Qilian and Kunlun Mountains (e.g., Molnar and Stock, 2009; Ding et al., 2022), as well as the mid-crustal channel flow and ductile extrusion of the Greater Himalaya (e.g., Mukherjee and Koyi, 2010; Mukherjee, 2013). One hypothesis suggests that the increasing elevation of the Tibetan plateau during the Miocene caused radially oriented compressive strain in the surrounding area, potentially influencing the transformation of the deep architecture of the Tian Shan (Molnar and Stock, 2009).

Moreover, understanding the geodynamic context of the foreland basins in terms of it being a retro- or pro-foreland basin aids hydrocarbon prospectivity in the basins (Bourrouilh et al., 1995; Naylor and Sinclair, 2008; Allen and Allen, 2013). For example, the rapid subsidence of the NTFB during the deposition of the Kuqa Formation resulted in the under-compaction, rapid hydrocarbon generation and significant increase in the residual pressure within the source rock formations in the Bozi-Dabei natural gas field within the basin (Yang et al., 2022; Wang et al., 2022). This pressure difference between the source and reservoir provided the dynamic for the migration of ultra-high-pressure natural gas into the reservoirs. The pro-foreland basin nature of the NTFB, influenced by its plate setting, determined the rapid and accelerating subsidence trend in the basin (Yang et al., 2022).

7.2 Implications of modelling on topographic growth

Our modelling of the subsidence process in the NTFB and SJFB predicts that the average elevations of the southern Tian Shan were no less than ~58% and ~77% of their present height at ~13.4 Ma and ~5.3 Ma, respectively; and the northern Tian Shan's average elevations were at least ~56%, ~75%, and ~87% of their present height at ~20.1 Ma, ~16.0 Ma, and ~4.7 Ma,

663 respectively (Figs. 8 and 9). Considering that the Mesozoic Tian Shan was dominated by low-
664 relief and small hills localized along discrete tectonic structures (Morin et al., 2019; He et al.,
665 2021b), our modelling results suggest that average elevations of both the southern and northern
666 Tian Shan had started to rise before the Miocene and reached half of their current average
667 elevation by the middle Miocene. This is in agreement with the continuous cooling and
668 exhumation in the region from the Eocene to Quaternary (e.g., Dumitru et al., 2001; Yu et al.,
669 2014; Chang et al., 2021), which is indicated by the available apatite fission track and zircon and
670 apatite (U-Th)/He ages varying from ~50 Ma to ~3 Ma in the region (Fig. 14) assuming a
671 constant value of geothermal gradient in the Tian Shan during the Cenozoic (Wang et al., 2023).
672 Hence, the topographic uplift before the middle Miocene could have contributed to the modern
673 mountain building of the middle segment of the Tian Shan. Our modelling also predicts that the
674 propagation rates of the northern Tian Shan wedge decreased by ~60% from ~16 Ma to ~5 Ma
675 compared with ~20–16 Ma (Fig. 11; Table 2). Considering that the pro-wedge of Alpine-type
676 orogenic belt has a faster extension rate than the retro-wedge in the growth stage (Ellis, 1996;
677 Vogt et al., 2017), this could also suggest that northern Tian Shan has transformed from a pro-
678 wedge to a retro-wedge after the middle Miocene.

679 The predicted average propagation rate of the southern and northern Tian Shan wedge from
680 ~5 Ma to the present is roughly double that of the period between ~12 and ~5 Ma, reflecting the
681 accelerated the uplift of the Tian Shan since ~5 Ma. This is in agreement with the continuous
682 acceleration of slip rates on thrust faults of the fold-thrust belts and sedimentation rates in the
683 foreland basins on both sides of the Tian Shan since the Quaternary (e.g., Sun et al., 2004; Huang
684 et al., 2006; Charreau et al., 2009; Lu et al., 2019; Li et al., 2023). The predicted acceleration of
685 the topographic growth is also consistent with the imbalance between an influx of material

686 (crustal thickening) and erosional efflux in the modern Tian Shan, the former outpaced the latter
687 by a factor of ~10 (Charreau et al., 2023).

688 The southern Tian Shan thrust wedge has been propagating at an average pace of ~2.2 mm/yr
689 since ~5 Ma, which is about twice as fast as the northern Tian Shan wedge (Table 2). This
690 difference in propagation rates between the southern and northern Tian Shan wedges agrees with
691 the characteristics of the propagated pattern of pro- and retro-wedges (Ellis, 1996; Vogt et al.,
692 2017). GPS observations (Zubovich et al., 2010; Shen and Wang, 2020) and balanced section
693 studies (Hubert-Ferrari et al., 2007) reflect that the frontal fold-and-thrust belt on the southern
694 piedmont of the southern Tian Shan (the current pro-wedge) absorbs most of the crustal
695 shortening in the wedge, suggesting that the range growth of the southern Tian Shan appears to
696 have been essentially sustained by frontal accretion of material from the crust of the Tarim block.
697 On the contrary, the northern Tian Shan's range growth, as the retro-wedge, could primarily be
698 supported by the uplift of the hinterland (Sun et al., 2022a). The distribution of the cooling ages
699 obtained in the same swath profile across the middle segment of the Tian Shan supports this
700 difference in the range growth pattern between the southern and northern Tian Shan thrust
701 wedges (Fig. 14), because samples with late Cenozoic cooling ages in the southern Tian Shan
702 were mainly obtained from the frontal edge of the thrust wedge, whereas those from the northern
703 Tian Shan were mainly taken from the hinterland region (Fig. 14). This reflects that the majority
704 of exhumation events in the southern Tian Shan region occurred at the frontal area of the wedge
705 as a typical pro-wedge, while those of the northern Tian Shan main occurred in its hinterland due
706 to its retro-wedge-style (Sinclair et al., 2005). Considering that δO^{18} isotopes and palynology in
707 the Tian Shan show a stable arid climate with stable low erosion since the Oligocene (Sun et al.,
708 2007; Macaulay et al., 2016; Jepson et al., 2021), the distribution of exhumation events reveals

that the frontal area of the southern Tian Shan wedge exhibits more active crustal shortening and uplift in comparison to its hinterland, whereas the reverse pattern is observed in the northern Tian Shan. In addition, the distribution of the cooling ages shows a southward migration of the strongest exhumation area in the southern Tian Shan towards the frontal of the wedge at ~12 Ma (Fig. 14), which may be related to enhanced lateral propagation of the southern Tian Shan thrust wedge as a result of transformation from a retro-wedge to a pro-wedge (Sun et al., 2022).

7.3 Implications on crustal shortening rates

The timing and velocity of crustal shortening absorbed by the Tian Shan can aid in understanding how deformation propagated from the southern Asian margin to remote intra-continental regions (Tapponnier et al., 1982, 2001; Neil and Houseman, 1997; Dayem et al., 2009), and paleomagnetism reveals a broad range of the crustal shortening between Tarim and Junggar lithospheres at 400±600 km (Chen et al., 1992). Based on the stratigraphic onlap rates in the NTFB and SJFB obtained from seismic profiles and the propagation rates of the southern and northern Tian Shan thrust wedges obtained from modelling results, we calculated the horizontal convergence rates between the Tarim and Junggar blocks since ~20 Ma, which represents the crustal shortening rates absorbed by the middle segment of the Tian Shan.

The crustal shortening rate absorbed by the Tian Shan was less than 2 mm/yr between 20–12 Ma (Fig. 11; Table 2) according to our calculations, which is only ~4% of the total convergence rate between the Indian and Eurasian continents during the same period (~50 mm/yr) as reconstructed by paleomagnetic data (Guillot et al., 2003; Copley et al., 2010). The oldest sedimentary sequence of the foreland succession in the NTFB was, deposited at ~26 Ma based on magnetostratigraphic constraints (Charreau et al., 2006; 2009; Huang et al., 2006), indicating that uplift of the modern Tian Shan was initiated no later than ~26 Ma (Li et al., 2019). Hence

732 the deformation caused by the India-Asia collision has already propagated to the Tian Shan by
733 the Oligocene. However, the majority of the crustal shortening during this period was absorbed
734 by the compressional and strike-slip structures in and around the Tibetan Plateau (Tapponnier et
735 al., 2001), leaving less than 4% of the total strain to be absorbed by the Tian Shan. The crustal
736 shortening rate of the Tian Shan increased to 10–14 mm/yr at ~12 Ma according to our
737 calculations, accounting for around 25–35% of the total convergence rate between the Indian and
738 Eurasian continents during the same period (~40 mm/yr) (Guillot et al., 2003; Copley et al.,
739 2010). Low-temperature thermochronological results from the Qilian Shan in the northeastern
740 margin of the Tibetan Plateau shows a similar fast tectonic uplift during the late Miocene (e.g.,
741 Zheng et al., 2010). These demonstrate that the intra-continental deformation brought on by the
742 India-Eurasia collision led to compressive strain which was radially orientated in the region
743 surrounding Tibet after the late Miocene (Molnar and Stock, 2009), and this region developed
744 into one of the most active tectonic zones. This kind of strain distribution mechanism tends to
745 transfer compressive stress to the areas in the northern Tibetan Plateau, (such as the Tian Shan),
746 and might also be related to the direct collision between the Indian lithospheric mantle and the
747 Tarim block (Huangfu et al., 2021), which resulted in strain concentration in the Tian Shan. The
748 range consequently absorbed a greater percentage of crustal shortening.

749 Furthermore, given the continuous Cenozoic sedimentary sequences observed in the foreland
750 basin systems on either side of the Qilian Shan orogen (Zuza et al., 2016), it is likely that our
751 research methods can be effectively employed to investigate the rates of crustal shortening and
752 the lithospheric architecture of the Qilian Shan in future studies.

7.4 The optimal *Te* and *β* values in numerical modelling results

Te is a key parameter in modelling lithospheric flexural deflection. In our model, the optimal *Te* values were determined by minimizing the misfits between the observed and predicted subsidence profiles. The optimal value of *Te* for the lithosphere of the modern Tarim and Junggar blocks obtained in our modelling is consistent with the predictions derived from gravity anomalies and geothermal data. The *Te* value for the Tarim block is 53 km, which is quite near to the median value of 66 ± 7 km as determined by the lithospheric thermo-rheological structure (Liu et al., 2006). The predicted *Te* value of 35 km for the Junggar block is slightly lower than that (40–50 km) obtained from the flexural and rheological modelling based on Bouguer gravity anomaly data (Jiang, 2014). Considering that our profile is located in the western segment of the Junggar Basin, this difference does not contradict Jiang's (2014) prediction of a decreasing trend of the *Te* value of the Junggar block from the basin center to the west.

In the case of no horizontal convergence, the predicted optimal values of *Te* for the Tarim and Junggar blocks both increased over the late Cenozoic. Many factors that affect lithospheric rheology (e.g., geothermal condition, lithospheric composition, and mechanical weakening) may be expressed through the *Te* (Burov and Diament, 1995). It is unclear why these lithosphere's *Te* values are rising, but the results are in line with the cooling process occurring in the Tarim and Junggar Basins. The paleogeothermal gradients in the Tarim Basin decreased slowly from ~2.7 to ~2.2 °C/100 m during the Paleogene to ~2.1 °C/100 m at present (Wang et al., 1995; Liu et al., 2006; Chang et al., 2017b), and the average heat flow of the Junggar Basin decreased from ~50 mW m^{-2} to ~42 mW m^{-2} from the Cretaceous to the present (Qiu et al., 2005). The *Te* values are sensitive to fluctuation in the heat flow when the average heat flow is between ~40 mW m^{-2} and ~70 mW m^{-2} (Hyndman et al., 2009; He et al., 2017). Considering an average heat flow of

776 ~44mW m^{-2} in the modern Tarim Basin (Hu et al., 2000; Liu et al., 2015), the cooling process
777 there may have been the primary factor contributing to the increase in the *Te* value. Moreover,
778 the optimal value of *Te* for the Tarim and Junggar blocks at ~20 Ma, ~13 Ma, and ~5 Ma is even
779 higher than the modern *Te* value in cases with maximum convergence distance, *C*. The decrease
780 in *Te* is contrary to the cooling process in the Tarim and Junggar Basin (Qiu et al., 2005; Liu et
781 al., 2006). These two predictions indicate that a larger convergence distance value leads to a
782 larger predicted optimal value of *Te*. Consequently, the main factor potentially responsible for
783 the abnormally high *Te* value is our possible overestimation of the convergence distance, *C*,
784 since ~20 Ma in the second end-member model. The value of *C* is equal to the cumulative
785 stratigraphic onlap distances, but this overlooks the onlap distance driven by the growth of the
786 thrust wedges. Thus, the adopted values were probably too high, resulting in abnormally high
787 values of *Te* from ~26 Ma to ~5 Ma. Nonetheless, if convergence is completely overlooked, the
788 *Te* values for the ancient Tarim and Junggar lithospheres may be underestimated.

789 The modelling based on the modern tectonic subsidence profile predicts a β value of ~7.8°
790 for the southern Tian Shan wedge, and it, together with the α value of 1.5° from the topographic
791 swath profile, constitute the wedge angle of 9.3°. The predicted β value of 7.0° and the observed
792 α value of 2.4° constitute the wedge angle of 9.4° for the northern Tian Shan wedge. A deep
793 seismic-reflection profile located ~600 km west of profile BB′ (~76°E) reflects that the dip angle
794 of the basal décollement fault beneath the junction of the southwestern Tian Shan and Tarim
795 block is ~8.0° (Gao et al., 2013), close to the predicted β value of the southern Tian Shan thrust
796 wedge at ~83°E derived from our modelling.

797 According to our modelling, the wedge angles of the southern and northern thrust wedges of
798 the Tian Shan are approximately equal, 9.3° and 9.4°, respectively. This is different from the

geometry of doubly vergent orogens predicted by the sandbox and numerical simulations, which has a significantly greater wedge angle for the retro-wedge than the pro-wedge (Vogt et al., 2017; Sun et al., 2022), such as the Alpine orogen in Europe (Sinclair et al., 2005; Schlunegger and Norton, 2015). This implies that both southern and northern Tian Shan could have undergone evolution stages of retro-wedge and pro-wedge, resulting in the similarity in their wedge angles. Specifically, when the Tarim block converged with the Tian Shan through lithosphere indentation before the middle Miocene, the southern Tian Shan was characterized by a retro-wedge, which tended to form a larger wedge angle, while the northern Tian Shan was characterized by a pro-wedge, that tended to form a smaller wedge angle. After the middle Miocene, the lithosphere subduction pattern replaced the convergence one, resulting in the formation of southern Tian Shan as a pro-wedge and the northern Tian Shan as a retro-wedge (Fig. 13). Consequently, the northern Tian Shan tended to form a relatively larger wedge angle, eventually leading to the current situation in which the wedge angles of the southern and northern Tian Shan are almost equal. It provides further validation for the transformation of the deep architecture of the Tian Shan revealed by the migration and subsidence histories of the coupled foreland basins.

8 Conclusions

The forelandward migration rates and subsidence history of the NTFB and SJFB are derived from the seismic profiles across these basins. The linear fitting of the upper envelope of the reflector terminations in profile AA′ displays that the forebulge of the SJFB migrated northward at ~3.1 mm/yr during the period of around 22-16 Ma. Based on the migration rates and observed subsidence profiles, we used an elastic numerical model to describe the evolution of tectonic subsidence in the foreland basins, combined with the formation of the southern and northern

Tian Shan wedges. The comparison between the migration and subsidence characters of NTFB and SJFB reveals their plate settings, which could test the three models of lithospheric architecture of the Tian Shan. Our analytical results and modelling show that the NTFB is characteristic of the plate setting of a retro-foreland basin, while the SJFB resembled a pro-foreland basin during the early-middle Miocene, which reveals the coeval uplift of the Junggar lithosphere and the indentation of the Tarim lithosphere beneath the Tian Shan. The plate setting of the NTFB and SJFB converted during the late Miocene to the present, implying a change in the subduction polarity of the Tarim and Junggar lithospheres. The convergence pattern between the Tarim lithosphere and the Tian Shan changed from lithospheric indentation to subduction, implying a change in the subduction polarity of the Tarim and Junggar lithospheres.

The modelling of the subsidence histories of the NTFB and SJFB also indicates that both the southern and northern Tian Shan had begun to uplift before the middle Miocene, with the orogen's height reached half of its present elevation before the late Miocene. The propagation rate of the northern Tian Shan has decreased since ~16 Ma, which may be related to the change of the subduction polarity of the Junggar block beneath the northern Tian Shan wedge. The propagation rates of the southern and northern Tian Shan have accelerated since the late Miocene. Besides, although the uplift of the modern Tian Shan was initiated at around 26 Ma, crustal shortening rate absorbed by the range was less than ~2 mm/yr between ~20 and ~12 Ma according to our calculations, which is only ~4% of the total convergence rate between the Indian and Eurasian continents during the same period. After the middle Miocene, it increased to ~10-14 mm/yr, accounting for ~25-35% of the total convergence rate, documenting that the Tian Shan has become one of the most active areas of intra-continental deformation in Asia since then.

Our research has revealed the subduction polarity of the Tarim and Junggar blocks beneath the middle segment of the Tian Shan. While the lateral variation of a lithospheric architecture along the range has not been fully constrained, our research provides valuable insights and information for understanding the lithospheric architecture of analogous complex intracontinental orogens. Moreover, understanding the plate setting characteristics of the two foreland basins could provide significant implications for hydrocarbon prospectivity.

Data Availability

The original seismic data supporting this research are owned by the China National Petroleum Corporation (CNPC) with commercial restrictions and are not accessible to the public or research community. The high-resolution seismic profiles used in this study can be accessed via: https://doi.org/10.6084/m9.figshare.22219000

Conflicts of Interest

The authors declare that they have no conflicts of interest.

Acknowledgements

This work was supported by the National Natural Science Foundation of China [grant numbers 42102250 and 42072153] and the second comprehensive scientific expedition to the Qinghai-Tibet Plateaus [grant number 2022QZKK0202]. Many thanks are given to Associate Editor Soumyajit Mukherjee and two anonymous reviewers for helpful comments and constructive suggestions.

References

[1] Aitken, A.R., 2011. Did the growth of Tibetan topography control the locus and evolution of Tien Shan mountain building?. *Geology*, 39, 459–462. http://dx.doi.org/10.1130/ G31712.1

[2] Bazhenov, M.L., Burtman, V.S., Dvorova, A., 1999. Permian paleomagnetism of the Tien Shan fold belt, Central Asia: post-collisional rotations and deformation. *Tectonophysics*, 312, 303–329. http://dx.doi.org/10.1016/S0040-1951(99)00181-X

[3] BGMRX (Bureau of Geological and Mineral Resources of BGMRX the Xinjiang Uygur Autonomous Region)., 1993. Regional geology of Xinjiang Uygur Autonomous region. Geology Publishing House, 1–841 p. (in Chinese)

[4] Bian, W.H., Hornung, J., Liu, Z.H., Wang, P.J., Hinderer, M., 2010. Sedimentary and palaeoenvironmental evolution of the Junggar Basin, Xinjiang, Northwest China. *Palaeobio Palaeoenv*, 90, 175–186. http://dx.doi.org/10.1007/s12549-010-0038-9

[5] Bourrouilh, R., Richert, J.P., & Zolnai, G., 1995. The North Pyrenean Aquitaine Basin, France-evolution and hydrocarbons. AAPG Bulletin, 79, 831–853. https://doi.org/10.1306/8D2B1BC4-171E-11D7-8645000102C1865D

[6] Bosboom, R.E., Dupont-Nivet, G., Houben, A.J.P., Brinkhuis, H., Villa, G., Mandic, O., Stoica, M., Zachariasse, W.J., Guo, Z.,J., Li, C.,X., Krijgsman, W., 2011. Late Eocene sea retreat from the Tarim Basin (west China) and concomitant Asian paleoenvironmental change. *Palaeogeography, Palaeoclimatology, Palaeoecology*, 299, 385–398. http://dx.doi.org/10.1016/j.palaeo.2010.11.019.

[7] Burov, E.B., Diament, M., 1992. Flexure of the continental lithosphere with multilayered rheology. *Geophysical Journal International*, 109, 449–468. http://dx.doi.org/10.1111/j.1365-246X.

[8] Burov, E., & Toussaint,G., 2007. Surface processes and tectonics . forcing of continental subduction and deep processes. *Global & Planetarv Change*, 58, 141-164. http://dx.doi.org/10.1016/j.gloplacha.2007.02.009

890 [9] Burbank, D. W., Beck, R. A., Raynolds, H., Hobbs, R., & Tahirkheli, K., 1988. Thrusting
891 and gravel progradation in foreland basins—A test of post-thrusting gravel dispersal. *Geology,*
892 16, 1143–1146. http://dx.doi.org/10.1130/0091-7613(1988)016<1143.TAGPIF>2.3.CO;2
893 [10] Burtman, V.S., 1975. Structural geology of the Variscan Tian Shan. *American Journal of*
894 *Science*, 275, 157–186.
895 [11] Calignano, E., Sokoutis, D., Willingshofer, E., Gueydan, F., Cloetingh, S., 2015. Strain
896 localization at the margins of strong lithospheric domains. insights from analog models.
897 *Tectonics*, 34, 396–412. http://dx.doi.org/10 .1002 /2014TC003756
898 [12] Capitanio, F., Morra, G., Goes, S. Weinberg, R.F., Moresi, L., 2010. India–Asia
899 convergence driven by the subduction of the Greater Indian continent. *Nature Geoscience*, 3,
900 136–139, http://dx.doi.org/10.1038/ngeo725
901 [13] Chang, J., Qiu, N.S., Xu, W., 2017b. Thermal regime of the Tarim basin, northwest
902 China. a review. *International Geology Review*, 59, 45–61.
903 http://dx.doi.org/10.1080/00206814.2016.1210546.
904 [14] Chang, J., Tian, Y.T., Qiu, N.S., 2017a. Mid-Late Miocene deformation of the northern
905 Kuqa fold-and-thrust belt (southern Chinese Tian Shan). An apatite (U-Th-Sm)/He study.
906 *Tectonophysics*, 694, 101-113. http://dx.doi.org/10.1016/j.tecto.2016.12.003
907 [15] Chang, J., Glorie, S., Qiu, N., Min, K., Xiao, Y., Xu, W., 2021). Late Miocene Ma) rapid
908 exhumation of the Chinese South Tianshan. Implications for the timing of aridification in the
909 Tarim Basin. *Geophysical Research Letters*, 48, e2020GL090623.
910 http://dx.doi.org/10.1029/2020GL090623
911 [16] Charreau, J., Gilder, S., Chen, Y., Dominguez, S., Avouac, J.P., Sen, S., Jolivet, M., Li,
912 Y.A., Wang, W.M., 2006. Magnetostratigraphy of the Yaha section, Tarim Basin (China). 11 Ma

913 acceleration in erosion and uplift of the Tian Shan Mountains. *Geology*, 34, 181–184.
914 http://dx.doi.org/10.1130/G22106.1
915 [17] Charreau, J., Chen, Y., Gumiaux, C., Gilder, S., Barrier, L., Dominguez, S., Augier, R.,
916 Sen, S., Avouac, J.-P., Gallaud, A., Graveleau, F., Wang, Q., 2009. Neogene uplift of the Tian
917 Shan Mountains observed in the magnetic record of the Jingou River section (northwest China).
918 *Tectonics*, 28, TC2008. http://dx.doi.org/10.1029/2007TC002137
919 [18] Charreau, J., Saint-Carlier, D., Dominguez, S., Lavé, J., Blard, P.H., Avouac, J.P.,
920 Jolivet, M., Chen, Y., Wang, S.L., Brown, N.D., Malatesta, L.C., Rhodes, E., 2017). Denudation
921 outpaced by crustal thickening in the eastern Tianshan. *Earth and Planetary Science Letters*,
922 479, 179-191. https://dx.doi.org/10.1016/j.epsl.2017.09.025.
923 [19] Charreau, J., Blard, P.H., Lavé, J., Dominguez, S., Wang, S.L., 2023. Unsteady
924 topography in the eastern Tianshan due to imbalance between denudation and crustal thickening.
925 *Tectonophysics*, 848, 229702. http://dx.doi.org/10.1016/j.tecto.2022.229702.
926 [20] Charvet. J., Shu, L.S, Laurent-Charvet, S., Wang, B., Faure, M., Cluzel, D., Chen, Y.,
927 DeJong, K., 2011. Palaeozoic tectonic evolution of the Tianshan belt, NW China. *Science China*
928 *Earth Sciences*, 54, 166–184. http://dx.doi.org/10.1007/s11430-010-4138-1
929 [21] Chen, Y., Cogné, J.P., Courtillot, (1992). New Cretaceous paleomagnetic poles from the
930 Tarim Basin, Northwestern China, *Earth and Planetary Science Letters*, 114, 17-38.
931 doi:10.1016/0012-821X(92)90149-P.
932 [22] Copley, A., Avouac, J.-P., and Royer, J.-Y., 2010. India-Asia collision and the Cenozoic
933 slowdown of the Indian plate. Implications for the forces driving plate motions. *Journal of*
934 *Geophysical Research-Solid Earth*, 115, B03410, http://dx.doi.org/10.1029/2009JB006634

[23] Davis, D., Suppe, J., Dahlen, F.A., 1983. Mechanics of fold and thrust belts and accretionary wedges. *Journal of Geophysical Research*, 88, 1153-1172. http://dx.doi.org/10.1029/JB088iB02p01153

[24] Dayem, E. K., Molnar, P., Clark, K. M., and Houseman, A. G., 2009. Far-field lithospheric deformation in Tibet during continental collision. *Tectonics*, 28, TC6005. http://dx.doi.org/10.1029/2008TC002344

[25] DeCelles, P. G., 2012. Foreland basin systems revisited: Variations in response to tectonic setting. In C. Busby, & A. Azor (Eds.), Tectonics of sedimentary basins: Recent advances (pp. 405–426): Blackwell Publishing Ltd. https://doi.org/10.1002/9781444347166

[26] DeCelles, P.G., & DeCelles, P.C., 2001. Rates of shortening, propagation, underthrusting, and flexural wave migration in continental orogenic systems. *Geology*, 29, p. 135–138. http://dx.doi.org/10.1130/0091-7613(2001)029<0135.ROSPUA>2.0.CO;2

[27] De Grave, J., Buslov, M.M., Van den haute, P., 2007. Distant effects of India-Eurasia convergence and Mesozoic intracontinental deformation in Central Asia. constraints from apatite fission-track thermochronology. *Journal of Asian Earth Sciences*, 29, 188–204. http://dx.doi.org/10.1016/j.jseaes.2006.03.001

[28] Deng, Q.D., Feng, X.Y., Zhang, P.Z., Yang, X.P., Xu, X.W., Peng, S.Z., Li, J., 1999. reverse fault and fold zone in the Urumqi range-front depression of the northern Tianshan and its genetic mechanism. *Earth Science Frontiers*, 6, 191–201. (in Chinese with English abstract) http://dx.doi.org/10.3321/j.issn.1005-2321.1999.04.001

[29] Ding, L., Kapp, P., Cai, F.L., Garzione, C.N., Xiong, Z.Y., Wang, H.Q., and Wang, C., 2022. Timing and mechanisms of Tibetan Plateau uplift. *Nature Reviews Earth & Environment*, 3, 652–667. http://dx.doi.org/10.1038/s43017-022-00318-4

[30] Dingle, E. H., Sinclair, H. D., Attal, M., Milodowski, D. T., & Singh., 2016. Subsidence control on river morphology and grain size in the Ganga Plain. *American Journal of Science*, 316, 778–812. http://dx.doi.org/10.2475/08.2016.03

[31] Du, Z.L., Wang, Q.C., 2007. Mesozoic and Cenozoic uplifting history of the Tianshan region. insight from apatite fission track. *Acta geological Sinica*, 81, 1082-1110. (in Chinese with English abstract)

[32] Du, Z. L., Wang, Q. C., Zhou, X. H., 2007. Mesozoic and Cenozoic uplifting history of the Kuqa-South Tianshan Basin-Mountain System from the evidence of apatite fission track analysis. *Acta Petrologica et Mineralogica*, 26, 399-408. (in Chinese with English abstract)

[33] Dumitru, T.A., Zhou, D., Chang, E.Z., Graham, S.A., Hendrix, M.S., Sobel, E.R., Caroll, A.R., 2001. Uplift, exhumation, and deformation in the Chinese Tian Shan. In. Hendrix, M.S., Davis, G.A. (Eds.. Paleozoic and Mesozoic tectonic evolution of central Asia. From continental assembly to intracontinental deformation. *Geological Society of America Memoir*, 194, 71–99. http://dx.doi.org/10.1130/0-8137-1194-0.71

[34] Ellis. S., 1996. Forces driving continental collision. reconciling indentation and mantle subduction tectonics. *Geology*, 24, 699-702. http://dx.doi.org/10.1130/0091-7613(1996)024<0699.FDCCRI>2.3.CO;2

[35] Gao, R., Hou, H, S., Cai, X, Y., Knapp, J. H., He, R, Z., Liu, J, K., Xiong, X, S., Guan, Y., Li, W, H., Zeng, L, S., Roecker, S, W., 2013. Fine crustal structure beneath the junction of the southwestern Tian Shan and Tarim Basin, NW China. *Lithosphere*, 5, 382–392. http://dx.doi.org/10.1130/L248.1

[36] Guillot, S., Garzanti, E., Baratoux, D., Marquer, D., Mahe´o, G., and de Sigoyer, J., 2003. Reconstructing the total shortening history of the NW Himalaya. *Geochemistry Geophysics Geosystems*, 4, 10-64, http://dx.doi.org/10.1029/2002GC000484.

[37] Gilligan, A., Roecker, S. W., Priestley, K. F., & Nunn, C., 2014. Shear velocity model for the Kyrgyz Tien Shan from joint inversion of receiver function and surface wave data. *Geophysical Journal International*, 199, 480–498. http://dx.doi.org/10.1093/gji/ggu225

[38] Guo, X.P., Ding, X.Z., He, X.X., Li, H.M., Su, X., Peng, Y., 2002. New progress in the study of marine transgressional events and marine strata of the Meso-Cenozoic in the Tarim Basin. *Acta Geologica Sinica*, 76, 299–307.

[39] He, D.F., Li, D., Fan, C., Yang, X.F., 2013. Geochronology, geochemistry and tectonostratigraphy of Carboniferous strata of the deepest Well Moshen-1 in the Junggar Basin, northwest China. Insights into the continental growth of Central Asia. *Gondwana Research*, 24, 560-577. http://dx.doi.org/10.1016/j.gr.2012.10.015

[40] He, Z.Y., Wang, B., Ni, X.H., De Grave, J., Scaillet, S., Chen, Y., Liu, J.S., Zhu, X., 2021a). Structural and kinematic evolution of strike-slip shear zones around and in the Central Tianshan. Insights for eastward tectonic wedging in the southwest Central Asian Orogenic Belt. *Journal of Structural Geology*, 144, 104279. http://dx.doi.org/10.1016/j.jsg.2021.104279.

[41] He, Z.Y., Wang, B., Nachtergaele, S., Glorie, S., Ni, X.H., Su, W.B., Cai, D.X., Liu, J.S., De Grave, J., 2021b). Long-term topographic evolution of the Central Tianshan (NW China) constrained by low-temperature thermochronology. *Tectonophysics*, 817, 229066. http://dx.doi.org/10.1016/j.tecto.2021.229066.

[42] Hendrix, M. S., Graham, S. A., Carroll, A. R., Sobel, E. R., Mcknight, C. L., Schulein, B. J., Wang, Z., 1992. Sedimentary record and climatic implications of recurrent deformation in the

Tian Shan. Evidence from Mesozoic strata of the north Tarim, south Junggar, and Turpan basins, northwest China. *Geological Society of America Bulletin*, 104, 53–79. http://dx.doi.org/10.1130/0016-7606(1992)104<0053.SRACIO>2.3.CO;2

[43] Homewood, P., Allen, P.A. and Williams, G.D., 1986. Dynamics of the Molasse Basin of western Switzerland, Foreland basins. 199–217 p. http://dx.doi.org/10.1002/9781444303810.ch10

[44] Hu, S.B., He, L.J., Wang, J.Y., 2000. Heat flow in the continental area of China. a new dataset. *Earth and Planetary Sciences Letters*, 179, 407–419. http://dx.doi.org/10.1016/S0012-821X(00)00126-6.

[45] Huang, B. C., Piper, J. D. A., Peng, S. T., Liu, T., Li, Z., Wang, Q. C., Zhu, R. X., 2006. Magnetostratigraphic and rock magnetic constraints on the history of Cenozoic uplift of the Chinese Tian Shan. *Earth and Planetary Science Letters*, 251, 346–364. http://dx.doi.org/10.1016/j.epsl.2006.09.020

[46] Huangfu, P.P., Li, Z.H., Zhang, K.J., Fan, W., Zhao, J., & Shi, Y.L., 2021. India-Tarim lithospheric mantle collision beneath western Tibet controls the Cenozoic building of Tian Shan. *Geophysical Research Letters*, 48, e2021GL094561. http://dx.doi.org/10.1029/2021GL094561

[47] Hubert-Ferrari, A., Suppe, J., Gonzalez-Mieres, R., Wang, W., 2007. Mechanisms of active folding of the landscape (southern Tian Shan, China). *Journal of Geophysical Research. Solid Earth*, 112, 1–39. http://dx.doi.org/10.1029/2006JB004362

[48] Hyndman, R.D., Currie, C.A., Mazzotti, S., Frederiksen, A., 2009. Temperature control of continental lithosphere elastic thickness, Te vs vs. *Earth and Planetary Science Letters*, 3–4, 539–548. http://dx.doi.org/10.1016/j.epsl.2008.11.023

[49] Jia, C.Z., Wei, G.Q., Wang, L.S., Jia, D., Guo, Z.J., 1997. Tectonic Characteristics and Petroleum, Tarim Basin, China. Beijing, Petroleum Industry Press, p. 200–295. (in Chinese)

[50] Jiang, X.D., (2014. Dynamic support of the Tien Shan lithosphere based on flexural and rheological modeling. *Journal of Asian Earth Sciences*, 93, 37–48. http.//dx.doi.org/10.1016/j.jseaes.2014.07.006

[51] Johnson, D.D., Beaumont, C., 1995. Preliminary results from a plan form kinematic model of Orogen evolution, surface processes and the development of Clastic Foreland Basin Stratigraphy, in Dorobek, S.L., & Ross, G.M., ed., Stratigraphic Evolution of Foreland Basins. Society of Economic Paleontologists and Mineralogists, Los Angeles, Special Publication 52, p. 3–24. http://dx.doi.org/10.2110/pec.95.52.0003

[52] Jolivet, M., Dominguez, S., Charreau, J., Chen, Y., Li, Y., Wang, Q.C., 2010. Mesozoic and Cenozoic tectonic history of the central Chinese Tian Shan. reactivated tectonic structures and active deformation. *Tectonics*, 29, TC6019. http://dx.doi.org/10.1029/2010TC002712

[53] Jepson, G., Glorie, S., Konopelko, D., Gillespie, J., Danišík, M., Mirkamalov, R., Mamadjanov, Y., & Collins, A. S., 2018). Low-temperature thermochronology of the Chatkal-Kurama terrane (Uzbekistan-Tajikistan). Insights into the Meso-Cenozoic thermal history of the western Tian Shan. *Tectonics*, 37, 3954-3969. http://dx.doi.org/10.1029/2017TC004878

[54] Laurent-Charvet, S., Charvet, J., Monié, P., Shu, L.S., 2003. Late Paleozoic strike-slip shear zones in eastern central Asia (NW China). new structural and geochronological data. *Tectonics*, 22, 1009. http://dx.doi.org/10.1029/2001TC901047

[55] Lei, J., & Zhao, D., 2007. Teleseismic P-wave tomography and the upper mantle structure of the central Tien Shan orogenic belt. *Physics of the Earth and Planetary Interiors*, 162, 165–185. http://dx.doi.org/10.1016/j.pepi.2007.04.010

[56] Li, C., Wang, S.L., Wang, L.S., 2019. Tectonostratigraphic history of the southern Tianshan, China. seismic profiling evidence. *Journal of Asian Earth Sciences*, 172, 101-114. http://dx.doi.org/10.1016/j.jseaes.2018.08.017

[57] Li, C., Wang, S.L., Naylor, M., Sinclair, H., Wang, L.S., 2020. Evolution of the Cenozoic Tarim Basin by flexural subsidence and sediment ponding. Insights from quantitative basin modelling. *Marine and Petroleum Geology*, 112, 104047. http://dx.doi.org/10.1016/j.marpetgeo.2019.104047.

[58] Li, C., Wang, S., Li, Y., Chen, Y., Sinclair, H., Wei, D., Ma, D.L., Lu, H.Y., Wang, X.Y., Wang, L.S., 2022a. Growth of the Tian Shan drives migration of the conglomerate-sandstone transition in the Southern Junggar foreland basin. *Geophysical Research Letters*, 49, e2021GL097545. http://dx.doi.org/10.1029/2021GL097545

[59] Li, C., Wang, S.L., Wang, Y.J., He, Z.Y., Wei, D.T., Jia, D., Chen, Y., Chen, G.H., Xue, F., Li, Y.J., 2022b. Modern Southern Junggar Foreland Basin System Adjacent to the Northern Tian Shan, Northwestern China. *Lithosphere*, (1. 7872549. http://dx.doi.org/10.2113/2022/7872549

[60] Li, D., Liang, D., Jia, C.Z., Wang, G., Wu, Q., He, D.F., 1996. Hydrocarbon accumulations in the Tarim Basin, China. *American Association of Petroleum Geologists Bulletin*, 80, 1587–1603. http://dx.doi.org/10.1306/64EDA0BE-1724-11D7-8645000102C1865D

[61] Li, F., Cheng, X., Chen, H., Shi, X., Li, Y., Charreau, J., & Weldon, R., 2023. Cenozoic shortening and propagation in the Eastern Kuqa fold-and-thrust belt, South Tian Shan, NW China. Tectonics, 42, e2022TC007447. https://doi.org/10.1029/2022TC007447

[62] Li, J. Y, Zhang, J., Zhao, X.X, Jiang, M., Li, Y.P., Zhu, Z.X., Feng, Q.W., Wang, L.J., Sun, G.H., Liu, J.F., Yang, T.N., 2016a. Mantle subduction and uplift of intracontinental

mountains. a case study from the Chinese Tianshan Mountains within Eurasia. *Scientific Reports*, 6, 28831. http://dx.doi.org/10.1038/srep28831

[63] Li, Q., Zhang, Y.Y., Dong, L., Guo, Z.J., 2018. Oligocene syndepositional lacustrine dolomite. A study from the Southern Junggar Basin, NW China. *Palaeogeography, Palaeoclimatology, Palaeoecology*, 503, 69-80. http://dx.doi.org/10.1016/j.palaeo.2018.04.004.

[64] Li, S.Q., Wang, X., Suppe, J., 2012. Compressional salt tectonics and synkinematic strata of the western Kuqa foreland basin, southern Tian Shan, China. *Basin Research*, 24, 475–497. http://dx.doi.org/10.1111/j.1365-2117.2011.00531.x

[65] Li, Y.J., Zhang, Q., Zhang, G.Y., Tian, Z.J., Peng, G.X., Qiu, B., Huang, Z.,B., Luo, J.,C., Wen, L., Zhao, Y., Jia, T.,G., 2016b. Cenozoic faults and faulting phases in the western Tarim Basin (NW China): effects of the collisions on the southern margin of the Eurasian plate. J. Asian Earth Sci. 132, 40–57. https://doi.org/10.1016/j.jseaes. 2016.09.018.

[66] Li, Z., Wang, D.X., Lin, W., Wang, Q.C., 2004. Mesozoic-Cenozoic clastic composition in Kuqa depression, northwest China. Implication for provenance types and tectonic attributes. *Acta Petrologica Sinica*, 20, 655–666. (in Chinese with English abstract)

[67] Li, Z.W., Roecker, S., Li, Z.H., Bin, W., Wang, H.T., Schelochkov, G., Bragin, (2009. Tomographic image of the crust and upper mantle beneath the western Tien Shan from the MANAS broadband deployment. possible evidence for lithospheric delamination. *Tectonophysics*, 477, 49–57. http://dx.doi.org/10.1016/j.tecto.2009.05.007

[68] Liu, J.L., Yang, X.Z., Liu, K.Y., Xu, Z.P., Jia, K., Zhou, L., Wei, H.X., Zhang, L., Wu, S.J., Wei, X.Z., 2023. Differential hydrocarbon generation and evolution of typical terrestrial gas-prone source rocks: An example from the Kuqa foreland basin, NW China. Marine and Petroleum Geology, 152, 106225. https://doi.org/10.1016/j.marpetgeo.2023.106225.

[69] Liu, S.W., Wang, L.S., Li, C., Zhang, P., Li, H., 2006. Lithospheric thermo-rheological structure and Cenozoic thermal regime in the Tarim basin, northwest China. *Acta Geologica Sinica*, 80, 344–350. (in Chinese with English abstract).

[70] Liu, S. W., Lei, X., and Wang, L. S., 2015. New heat flow determination in northern Tarim Craton, northwest China. *Geophysical Journal international*, 200, 1194–1204. http://dx.doi.org/10.1093/gji/ggu458

[71] Lu, H.F., Howell, D. G., Jia, D., Cai, D. S, Wu, S. M., Chen, C. M., Shi, Y. S., Valin, Z. C., 1994. Rejuvenation of the Kuqa foreland basin, northern flank of the Tarim basin, northwest China. *International Geology Review*, 36, 1151–1158. http://dx.doi.org/10.1080/00206819409465509

[72] Lu, H.H., Burbank, W.D., Li, Y.L., Liu, Y.M., 2010. Late Cenozoic structural and stratigraphic evolution of the northern Chinese Tian Shan foreland. *Basin Research*, 22, 249–269. http://dx.doi.org/10.1111/j.1365-2117.2009.00412.x

[73] Lv, R., 2005. The relationship between tectonic evolution of intracontinental foreland basin and Oil-gas in southern margin of Junggar Basin [Master's dissertation, in Chinese with English Abstract]. Beijing, China University of Geosciences, 28 p.

[74] Lü, Z., Gao, H., Lei, J., Yang, X., Rathnayaka, S., & Li, C., 2019. Crustal and upper mantle structure of the Tien Shan orogenic belt from full-wave ambient noise tomography. *Journal of Geophysical Research. Solid Earth*, 124(4. 3987–4000. http://dx.doi.org/10.1029/2019JB017387

[75] Lyon-Caen, H., and Molnar, P., 1985. Gravity anomalies flexure of the Indian plate and the structure support and evolution of the Himalaya and Ganga Basin. *Tectonics*, 4, 513–538. http://dx.doi.org/10.1029/TC004i006p00513

[76] Jiang, X.D., 2014). Dynamic support of the Tien Shan lithosphere based on flexural and rheological modelling. Journal of Asian Earth Sciences, 93, p. 37–48. http://dx.doi.org/10.1016/j.jseaes.2014.07.006.

[77] Kapp, P. & DeCelles, P. G., 2019. Mesozoic–Cenozoic geological evolution of the Himalayan–Tibetan orogen and working tectonic hypotheses. American Journal of Science, 319, 159–254. https://doi.org/10.2475/03.2019.01

[78] Macaulay, E. A., Sobel, E. R., Mikolaichuk, A., Wack, M., Gilder, S. A., Mulch, A., Fortuna, A.B., Hynek, S., Apayarov, F., 2016. The sedimentary record of the Issyk Kul basin, Kyrgyzstan: Climatic and tectonic inferences. *Basin Research*, 28(1), 57–80. https://doi.org/10.1111/bre.12098

[79] Makeyeva, L.I., Vinnik, L.P., Roecker, S.W., 1992. Shear-wave splitting and small scale convection in the continental upper mantle. *Nature*, 358, 144–147. http://dx.doi.org/10.1038/358144a0

[80] Molnar, P., & Tapponnier, P., 1975. Cenozoic tectonics of Asia. Effects of a continental collision. *Science*, 189, 419–426. http://dx.doi.org/10.1126/science.189.4201.419

[81] Molnar, P., Stock, J.M., 2009. Slowing of India's convergence with Eurasia since 20 Ma and its implications for Tibetan mantle dynamics. *Tectonics*, 28, TC3001. http://dx.doi.org/10.1029/2008TC002271

[82] Morin, J., Jolivet, M., Barrier, L., Laborde, A., Li, H.B., Dauteuil, O., 2019. Planation surfaces of the Tian Shan Range (Central Asia). Insight on several 100 million years of topographic evolution. *Journal of Asian Earth Sciences*, 177, 52-65. http://dx.doi.org/10.1016/j.jseaes.2019.03.011.

[83] Mukherjee, S., Koyi, H.A., 2010. Higher Himalayan Shear Zone, Sutlej section: structural geology and extrusion mechanism by various combinations of simple shear, pure shear and channel flow in shifting modes. *International Journal of Earth Sciences*, 99, 1267–1303. https://doi.org/10.1007/s00531-009-0459-8

[84] Mukherjee, S., 2013. Channel flow extrusion model to constrain dynamic viscosity and Prandtl number of the Higher Himalayan Shear Zone. *International Journal of Earth Sciences*, 102, 1811–1835. https://doi.org/10.1007/s00531-012-0806-z

[85] Neil, E. A., & Houseman, G. A., 1997. Geodynamics of the Tarim basin and the Tianshan in central Asia. *Tectonics*, 16, 571–584. http://dx.doi.org/10.1029/97TC01413

[86] Naylor, M., & Sinclair, H. D., 2008. Pro-vs. Retro-foreland basins. *Basin Research*, 20, 285–303. http://dx.doi.org/10.1111/j.1365-2117.2008.00366.x

[87] Qi, J.F., Li, Y., Wu, C., Yang, S.J., 2013. The interpretation models and discussion on the contractive structure deformation of Kuqa Depression, Tarim Basin. *Geology in China*, 40, 106–120. (in Chinese with English abstract)

[88] Qiu, N.S, Zha, M., Wang, X., and Yang H.B (2005. Tectono-thermal evolution of the Junggar Basin, NW China. constraints from Ro and apatite fission track modelling. *Petroleum Geoscience*, 11, 361-372. http://dx.doi.org/10.1144/1354-079304-655

[89] Roecker, S.W., Sabitova, T.M., Vinnik, L.P., Burmakov,Y., Golvanov,M., Mamatkanova,R., Munirova L., 1993. Three-Dimensional elastic wave velocity structure of the western and central Tian Shan. *Journal of Geophysical Research*, 98, 15779–15795. http://dx.doi.org/10.1029/93JB01560

[90] Saura, E., Garcia-Castellanos, D., Casciello, E., Parravano, V., Urruela, A., Vergés, J., 2015. Modelling the flexural evolution of the Amiran and Mesopotamian foreland basins of NW Zagros (Iran-Iraq). *Tectonics*, 34(3. 377-395. http://dx.doi.org/10.1002/2014TC003660

[91] Sclater, J.G., Christie, P.A.F., 1980. Continental stretching. an explanation of the postmid-Cretaceous subsidence of the central North Sea basin. *Journal of Geophysical Research*, 85, 3711–3739. http://dx.doi.org/10.1029/JB085iB07p03711.

[92] Schlunegger, F., & Norton, K., 2015. Climate vs. tectonics. The competing roles of Late Oligocene warming and Alpine orogenesis in constructing alluvial megafan sequences in the North Alpine foreland basin. *Basin Research*, 27, 230–245. http://dx.doi.org/10.1111/bre.12070.

[93] Shao, L.Y., He, Z.P., Gu, J.Y., Luo, W.L., Jia, J.H., Liu, Y.F., Zhang, P., 2006. Lithofacies paleogeography of the Paleogene in Tarim basin. *Journal of Paleogeography*, 8, 353–364 (in Chinese with English Abstract).

[94] Simoes, M., Avouac, P.J., 2006. Investigating the kinematics of mountain building in Taiwan from the spatiotemporal evolution of the foreland basin and western foothills. *Journal of Geophysical Research*, 111, B10401. http://dx.doi.org/10.1029/2005JB004209

[95] Sinclair, H.D., Gibson, M., Naylor, M., Morris, R.G., 2005. Asymmetric growth of the Pyrenees revealed through measurement and modeling of orogenic fluxes. American Journal of Science, 305, 369 – 406. https://doi.org/10.2475/ajs.305.5.369

[96] Sinclair, H. D., & Naylor, M., 2012. Foreland basin subsidence driven by topographic growth versus plate subduction. *Geological Society of America Bulletin*, 124, 368–379. http://dx.doi.org/10.1130/B30383.1

[97] Steffen, R., Steffen, H., Jentzsch, G., 2011. A three-dimensional Moho depth model for the Tien Shan from EGM2008 gravity data. *Tectonics*, 30, TC5019. http://dx.doi.org/10.1029/2011TC002886

[98] Sun, C., Li, Z.G., Zuza, A.V., Zheng, W.J., Jia, D., He, Z.Y., Hui, G., Yang, S., 2022a. Controls of mantle subduction on crustal-level architecture of intraplate orogens, insights from sandbox modelling. *Earth and Planetary Science Letters*, 584, 117476. http://dx.doi.org/10.1016/j.epsl.2022.117476.

[99] Sun, W.J., Ao, S.J., Tang, Q.Y., Malusà, M.G., Zhao, L., Xiao, W.J., 2022b. Forced Cenozoic continental subduction of Tarim craton-like lithosphere below the Tianshan revealed by ambient noise tomography. *Geology*, 50, 1393–1397. http://dx.doi.org/10.1130/G50510.1

[100] Sun, J.M., Zhu, R.X., Bowler, J., 2004. Timing of the Tianshan Mountains uplift constrained by magnetostratigraphic analysis of molasse deposits. *Earth and Planetary Science Letters*, 219, 239–253. http://dx.doi.org/10.1016/S0012-821X(04)00008-1

[101] Sun, J.M., Xu, Q.H., Huang, B.C., 2007. Late Cenozoic magnetochronology and paleoenvironmental changes in the northern foreland basin of the Tian Shan Mountains. Journal of Geophysical Research, 112, B04107.

[102] Tapponnier, P., Peltzer, G., Dain, A., Armijo, R., Cobbold, P., 1982. Propagating extrusion tectonics in Asia. new insights from simple experiments with plasticine. *Geology*, 10, 608–611. http://dx.doi.org/10.1130/0091-7613(1982)10<611.PETIAN >2.0.CO;2.

[103] Tapponnier, P., Xu, Z., Roger, F., Meyer, B., Arnaud, N., Wittlinger, G., Yang, J., 2001. Oblique stepwise rise and growth of the Tibet Plateau. *Science*, 294, 1671–1677. http://dx.doi.org/10.1126/science.105978

[104] Vogt, K., Willingshofer, E., Matenco, L., Sokoutis, D., Gerya, T., Cloetingh, S., 2017. The role of lateral strength contrasts in orogenesis. a 2d numerical study. *Tectonophysics*, 746, 549–561. http://dx.doi.org/10.1016/j.tecto.2017.08.010.

[105] Wang, B., Chen, Y., Zhan, S., Shu, L., Faure, M., Cluzel, D., Charvet, J., Laurent-Charvet, S., 2007. Primary Carboniferous and Permian paleomagnetic results from the Yili Block (NW China) and their implications on the geodynamic evolution of Chinese Tianshan belt. *Earth and Planetary Science Letters*, 263, 288–308. http://dx.doi.org/10.1016/j.epsl.2007.08.037

[106] Wang, Q.C, Li, S., Du, Z.L., 2009. Differential uplift of the Chinese Tianshan since the Cretaceous. constraints from sedimentary petrography and apatite fission-track dating. *International Journal of Earth Sciences*, 98, 1341–1363. http://dx.doi.org/10.1007/s00531-009-0436-2

[107] Wang, Q.C, Zhang, P.-Z., Freymueller, J.T., Bilham, R., Larson, K.M., Lai, X., You, X., Niu, Z., Wu, J., Li, Y., Liu, J., Yang, Z., Chen, Q., 2001b. Present-day crustal deformation in China constrained by global positioning system measurements. *Science*, 294, 574–577. http://dx.doi.org/10.1126/science.1063647.

[108] Wang, S.J., He, L.J., Wang, J.Y., 2001a. Thermal regime and petroleum systems in Junggar basin, northwest China. *Physics of the Earth and Planetary Interiors*, 126, 237–248. http://dx.doi.org/10.1016/S0031-9201(01)00258-8

[109] Wang, L.S., Li, C., Shi, Y.S., 1995. The distribution characteristics of heat flow densities in Tarim Basin. *Science China*, 38, 855–856 (in Chinese).

[110] Wang, M., Shen, Z.K., 2020. Present-day crustal deformation of continental China derived from GPS and its tectonic implications. *Journal of Geophysical Research. Solid Earth*, 125, e2019JB018774. http://dx.doi.org/10.1029/2019JB018774.

[111] Wang, S.L., Chen, Y., Charreau, J., Wei, D. T., Jia, D., 2013. Tectono-stratigraphic history of the Southern Junggar Basin. seismic profiling evidences. *Terra Nova*, 25, 490–495. http://dx.doi.org/10.1111/ter.12063

[112] Wang, X., Suppe, J., Guan, S. W., Hubert-Ferrari, A., Gonzalez-Mieres, R., Jia, C. Z., 2011. Cenozoic structure and tectonic evolution of the Kuqa fold belt, southern Tianshan, China. *American Association of Petroleum Geologists Memoir*, 94, 215–243. http://dx.doi.org/10.1306/13251339M94389

[113] Wang, Y.J., Jia, D., Pan, J.G., Wei, D.T., Tang, Y., Wang, G.D., Wei, C.R., Ma, D.L., 2018. Multiple-phase tectonic superposition and reworking in the Junggar Basin of northwestern China—Implications for deepseated petroleum exploration. *AAPG Bulletin*, 102, 1489–1521. http://dx.doi.org/10.1306/10181716518

[114] Wang, Y.N., Zhang, J., Huang, X., Wang, Z.J., 2023. Cenozoic exhumation of the Tianshan as constrained by regional low-temperature thermochronology. *Earth-Science Reviews*, 237, 104325. http://dx.doi.org/10.1016/j.earscirev.2023.104325

[115] Wang, Z., Li, T., Zhang, J. Liu, Y.Q., Ma, Z.J., 2008. The uplifting process of the Bogda Mountain during the Cenozoic and its tectonic implication. *Science China. Earth Sciences*, 51, 579–593. http://dx.doi.org/10.1007/s11430-008-0038-z

[116] Wickert, A.D., 2016. Open-source modular solutions for flexural isostasy. gflex v1.0. *Geosci. Model De(GMD.* 9, 997–1017. http://dx.doi.org/10.5194/gmd-9-997-2016.

[117] Windley, B.F., Allen, M.B., Zhang, C., Zhao, Z.Y., Wang, G.R., 1990. Paleozoic accretion and Cenozoic deformation of the Chinese Tien Shan Range, central Asia. *Geology*, 18, 128–131. http://dx.doi.org/10.1130/0091-7613(1990)018<0128.PAACRO>2.3.CO;2

[118] Wright, M.H., 1996. Direct Search Methods. Once Scorned, Now Respectable, in Griffiths, D.F., and Watson, G.A., Eds., Numerical Analysis 1995, Proceedings of the 1995 Dundee Biennial Conference in Numerical Analysis, Addison Wesley Longman, Harlow, UK (191–208 p.

[119] Wu, C.Y., Wu, G.D., Shen, J., Dai, X.Y., Chen, J.B., Song, H.P., 2016. Late Quaternary tectonic activity and crustal shortening rate of the Bogda mountain area, eastern Tian Shan, China. *Journal of Asian Earth Sciences*, 119(1. 20–29. http://dx.doi.org/10.1016/j.jseaes.2016.01.001.

[120] Wu, C.Y, Zhang, P.Z., Zhang, Z., et al., (2023. Slip partitioning and crustal deformation patterns in the Tianshan orogenic belt derived from GPS measurements and their tectonic implications. *Earth-Science Reviews*, 238, 104362. https.//doi:org/10.1016/j.earscirev.2023.104362

[121] Xiao, W., Windley, B. F., Allen, M. B., Han, C., 2013. Paleozoic multiple accretionary and collisional tectonics of the Chinese Tianshan orogenic collage. *Gondwana Research*, 23, 1316–1341. http://dx.doi.org/10.1016/j.gr.2012.01.012

[122] Yang, S.F., Chen, H.L., Chen, X.G., Xiao, A.C., Zhou, Y.Z., Lu, H.F., Jia, C.Z., Wei, G.Q., 2003. Cenozoic uplifting and unroofing of southern Tien Shan, China. Journal of Nanjing University (Natural Sciences. 39, p. 1–8. (in Chinese with English abstract)

[123] Yang, W., Jolivet, M., Dupont-Nivet, G., Guo, Z., Zhang, Z., Wu, C., 2013. Source to sink relations between the Tian Shan and Junggar Basin (northwest China) from Late Palaeozoic to Quaternary. Evidence from detrital U-Pb zircon geochronology. *Basin Research*, 25, 219–240. http://dx.doi.org/10.1111/j.1365-2117.2012.00558.x

[124] Yang, X.W., Wang, Q.H., Li, Y., Lv, X.X., Xie, H.W., Wu, C., Wang, C.L., Wang, X., Mo, T., Wang, R., 2022. Formation mechanism of the Bozi-Dabei trillion cubic natural gas field Kuqa foreland thrust belt. Earth Science Frontiers , 29(6), 175-187. (in Chinese with English abstract) https://doi.org/10.13745/i.esf.sf,2022,8,18

[125] Yang, Y., & Liu, M., 2002. Cenozoic deformation of the Tarim plate and the implications for mountain building in the Tibetan plateau and the Tian Shan. *Tectonics*, 21, 1059. http://dx.doi.org/10.1029/2001TC001300

[126] Yin, A., Nie, S., Craig, P., Harrison, T.M., Ryerson, F.J., Qian, X., Yang, G., 1998. Late Cenozoic tectonic evolution of the southern Chinese Tian Shan. *Tectonics*, 17, 1–27. http://dx.doi.org/10.1029/97TC03140

[127] Yu, S., Chen, W., Evans, N.J., McInnes, B.A., Yin, J., Sun, J., 2014. Cenozoic uplift, exhumation and deformation in the north Kuqa depression, China as constrained by (U-Th)/He thermochronometry. *Tectonophysics*, 630, 166–182. http://dx.doi.org/10.1016/j.tecto.2014.05.021

[128] Zhang, B., Bao, X., Xu, Y., 2020. Distinct orogenic processes in the south- and north-central Tien Shan from receiver functions. Geophysical Research Letters, 47, e2019GL086941. http://dx.doi.org/10.1029/2019GL086941

[129] Zhang, S., Huang, Z., Zhu, H., 2004). Phanerozoic Stratigraphy in Covered Area of Tarim Basin. Beijing, Petroleum Industry Press, 1–300 p. (in Chinese)

[130] Zhang, T., Fang, X., Song, C., Appel, E., Wang, Y., 2014. Cenozoic tectonic deformation and uplift of the south Tian Shan. implications from magnetostratigraphy and balanced cross-section restoration of the Kuqa depression. *Tectonophysics*, 628, 172–187. http://dx.doi.org/10.1016/j.tecto.2014.04.044

[131] Zhang, Z. C., Guo, Z. J., Wu, C. D., & Fang, S. H., 2007. Thermal history of the Jurassic strata in the Northern Tianshan and its geological significance, revealed by apatite fission-track and vitrinite-reflectance analysis. *Acta Petrologica Sinica*, 23, 1683–1695. (in Chinese with English abstract)

[132] Zhao, J.M., Chen, S.Z., Zhang, H., Liu, H.B., Shao, X.Z., Chen, X.F., Xu, J., Ma, Z.J., 2019. Lithospheric structure beneath the eastern Junggar Basin (NW China. inferred from velocity, gravity and geomagnetism. *Journal of Asian Earth Sciences*, 177, 295–306. http://dx.doi.org/10.1016/j.jseaes.2019.03.026

[133] Zhao, J. M., Liu, G., Lu, Z., Zhang, X., Zhao, G., 2003. Lithospheric structure and dynamic processes of the Tianshan orogenic belt and the Junggar basin. *Tectonophysics*, 376, 199–239. http://dx.doi.org/10.1016/j.tecto.2003.07.001

[134] Zheng, D.W., Clark, M.K., Zhang, P.Z., Zheng, W.J., Farley, K.A., 2010. Erosion, fault initiation and topographic growth of the North Qilian Shan (northern Tibetan Plateau). *Geosphere*, 6, 937–941. http://dx.doi.org/10.1130/GES00523.1

[135] Zubovich, A. V., Wang, X., Scherba, Y. G., Schelochkov, G. G., Reilinger, R., & Reigber, C., Mosienko, O., Molnar, P., Michajljow, W., Makarov, V, I., Li, J., Kuzikov, S, I., Herring, T, A., Hamburger, M, W., Hager, B, H., Dang, Y. M., Bragin, V, D., Beisenbaev, R, T., 2010. GPS velocity field for the Tien Shan and surrounding regions. *Tectonics*, 29, TC6014. http://dx.doi.org/10.1029/2010TC002772

[136] Zuza, A.V., Cheng, X., Yin, A., 2016. Testing models of Tibetan Plateau formation with Cenozoic shortening estimates across the Qilian Shan-Nan Shan thrust belt. *Geosphere*, 12, 501–532. http://dx.doi.org/10 .1130 /GES01254 .1.

Figure 1

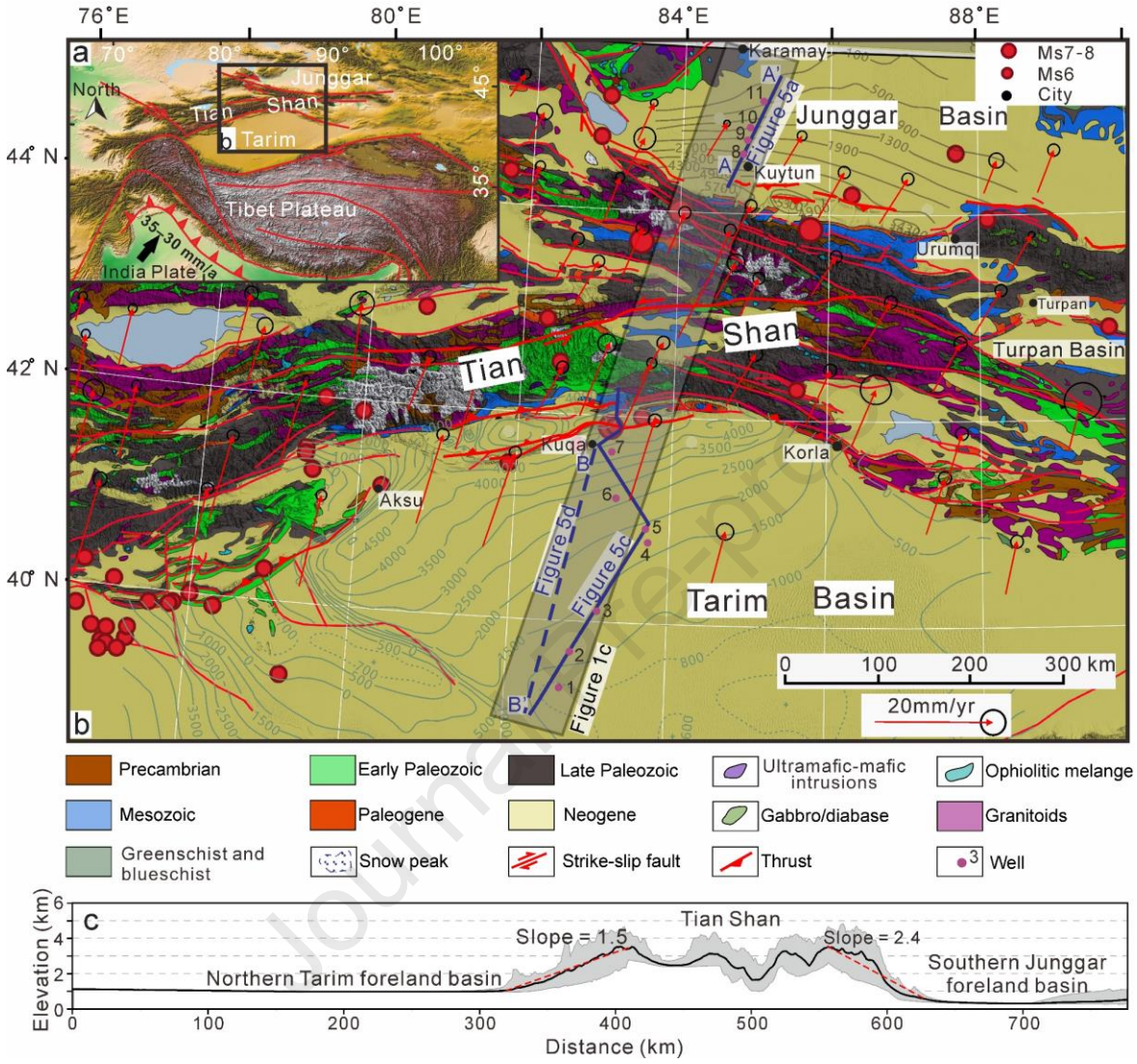

Figure 1 (a) The Tian Shan in the India-Asia collisional system. The direction and velocity of the Indian tectonic plate is from Wang et al. (2001b). (b) Geological map of the middle segment of the Tian Shan and the bilateral foreland basins on its southern and northern sides. The faults are drawn from Wu et al. (2016). Thickness contours (unit: m) of the Neogene successions in the NTFB and the SJFB are from Jia et al. (1997) and Lv (2005), respectively. The solid dark blue line is the north-northeast trending seismic profile across the NTFB and SJFB. The dashed dark blue line marks the location of the projected section of the seismic profile across the NTFB. The red arrows show the GPS velocity field in the Tian Shan with respect to stable Eurasia, and the GPS data with the error ellipses representing 70% confidence are from Wang and Shen (2020). (c) A topographic swath profile across the Tian Shan, NTFB and SJFB (see Fig. 1b for location).

Figure 2

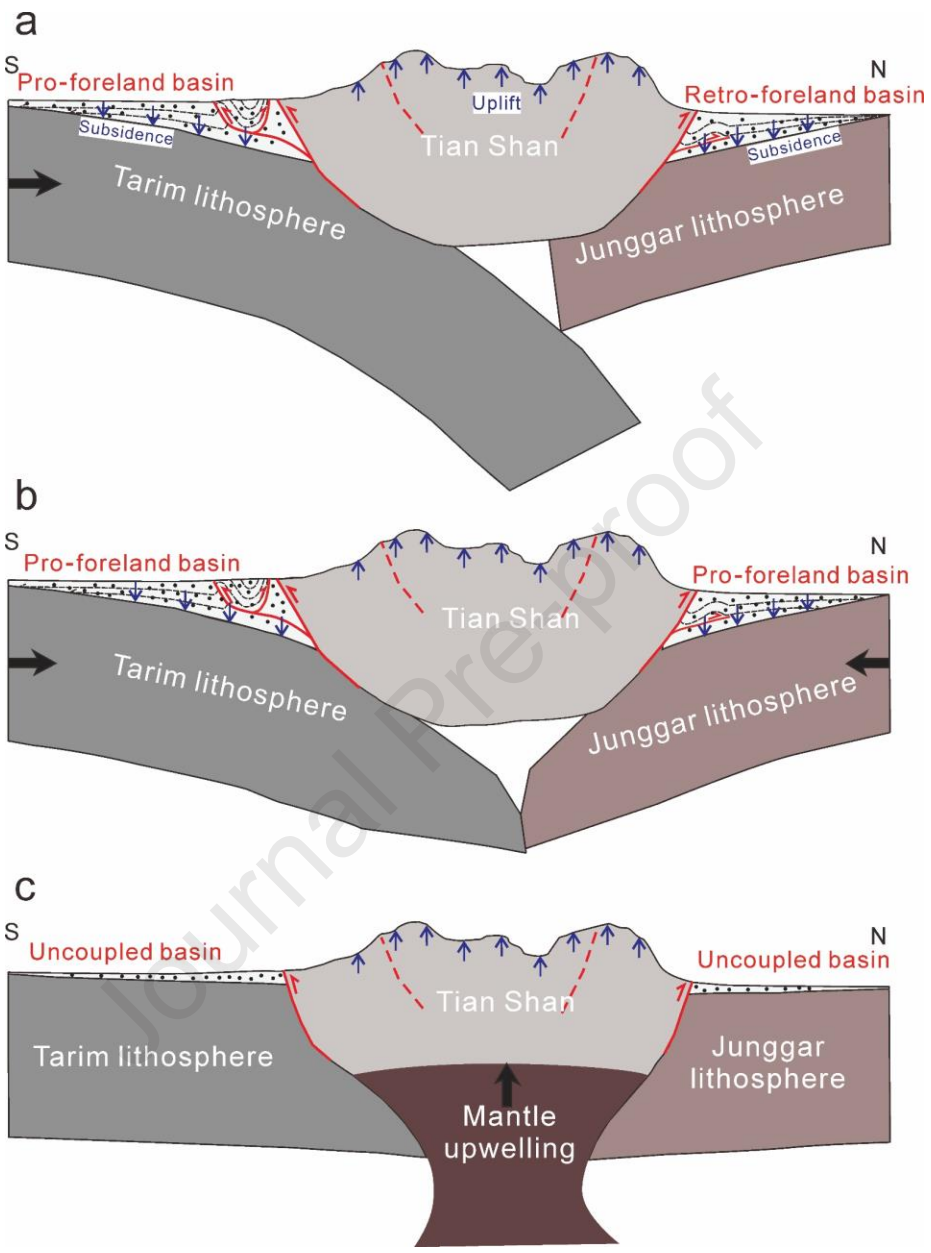

Figure 2 Schematic diagrams illustrating the three models of the lithospheric architecture of the Tian Shan. (a) The Tarim lithosphere underthrusts beneath the Junggar lithosphere (Zhao et al., 2003; Steffen et al., 2011; Gilligan et al., 2014). (b) The bidirectional underthrusting of the Tarim and Junggar lithospheres contributed to the topographic growth of the Tian Shan (Li et al., 2016a; Lü et al., 2019). (c) Mantle upwelling played a significant role in Tian Shan's uplift (Roecker et al., 1993; Lei and Zhao, 2007).

Figure 3

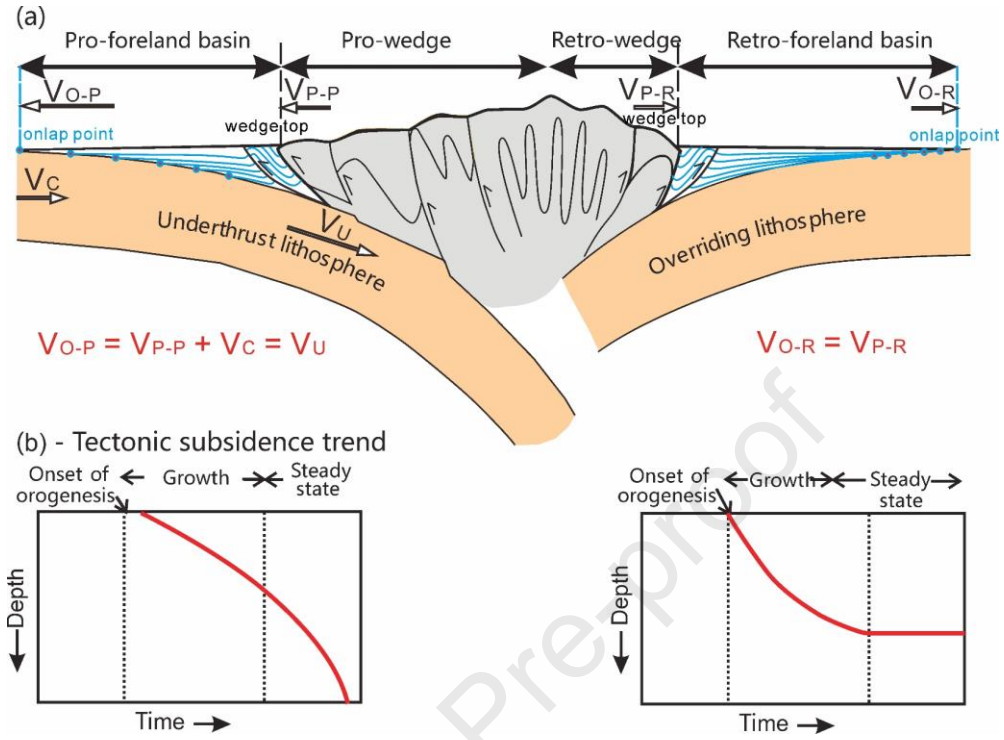

Figure 3 (a) The contrasting characteristics of pro-/retro-foreland basins (modified after Naylor and Sinclair, 2008; Sinclair and Naylor, 2012). The pro-foreland foreland basin exhibits significant basin onlap of the underthrust lithosphere, at a rate $V_{O\text{-}P}$ equal to the sum of the plate convergence rate V_C and the propagation rate of the pro-wedge $V_{P\text{-}P}$; in contrast, the retro-foreland basin records little onlap except in the early stage of growth. Its onlap rate $V_{O\text{-}R}$ is equal to the propagation rate of the retro-wedge $V_{P\text{-}R}$. (b) The pro-foreland basin records accelerated subsidence over a relatively short interval of orogenesis. In contrast, the retro-foreland basin records the full history of the basin with initial uniform subsidence during the growth of the mountain range.

Figure 4

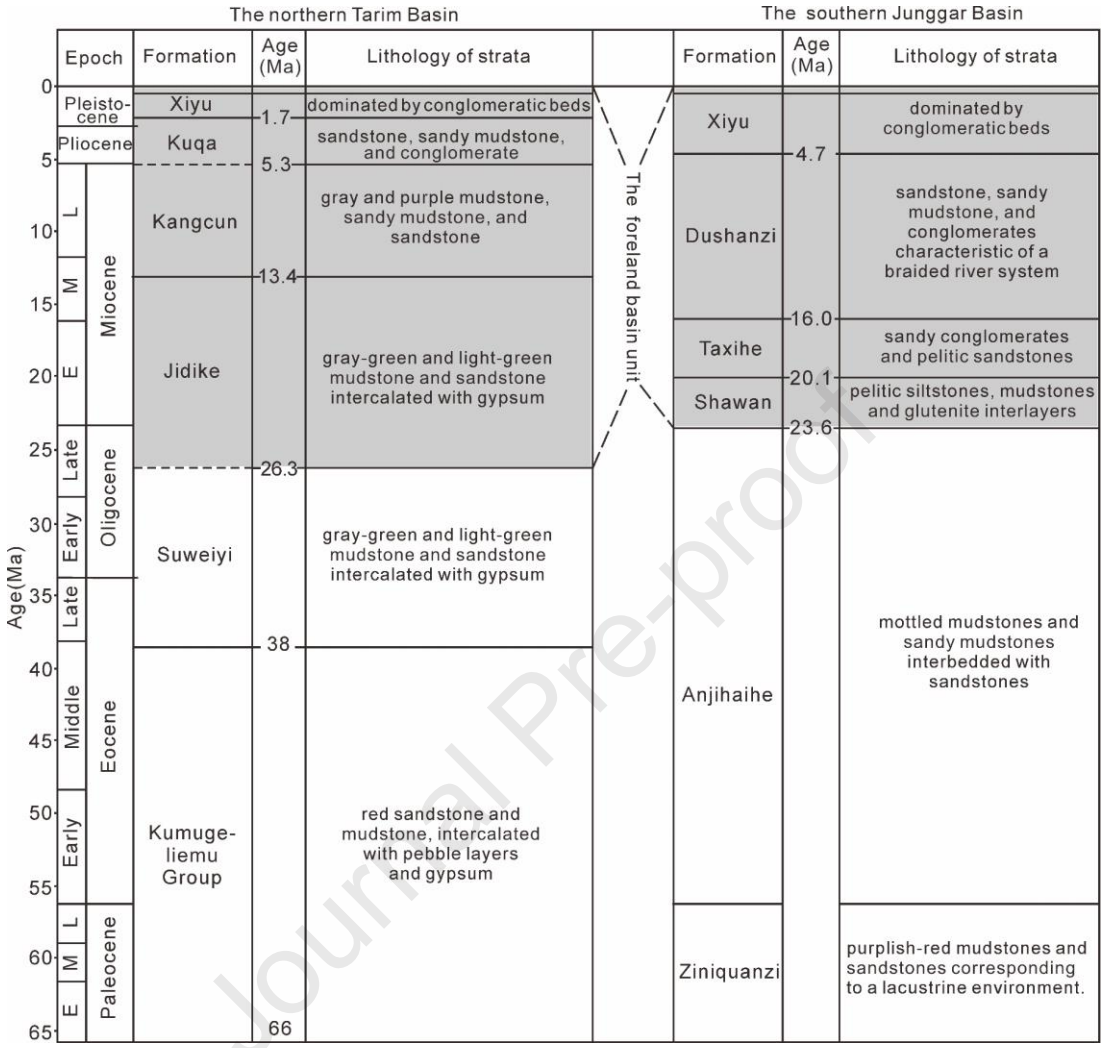

Figure 4 Simplified lithostratigraphic charts of the NTFB and SJFB. The lithology of each formation is summarized by Zhang et al. (2004) and Yang et al. (2013). The ages of formations in the basins are constrained by magnetostratigraphic studies (Huang et al., 2006; Charreau et al., 2009; Lu et al., 2010; Zhang et al., 2014). The dotted lines indicate the unconformities between the formations.

Figure 5

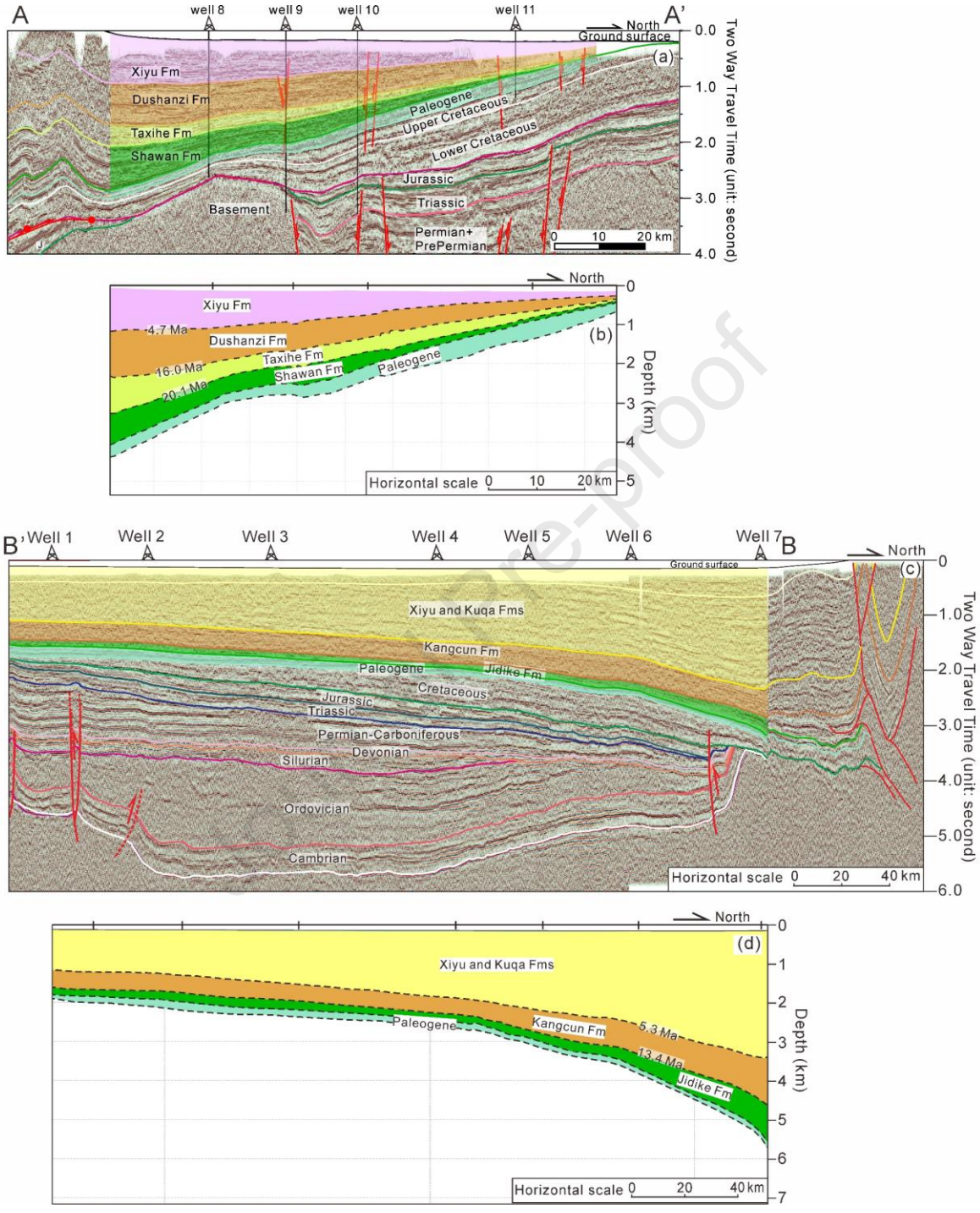

Figure 5 The interpreted north-northeast trending seismic profiles across the SJFB (a) and the NTFB (c). See Figure 1b for their locations. Vertical exaggeration is ~15 times. These boundaries and faults are interpreted from well logging data near the profiles and interpretations of other seismic reflection profiles

near the profiles from previous publications (Wang et al., 2013; Yu et al., 2014; Li et al., 2019). (b) The depth section of Figure 5c. (d) The projected depth section of the foredeep part in Figure 5a. See Figure 1b for its location.

Figure 6

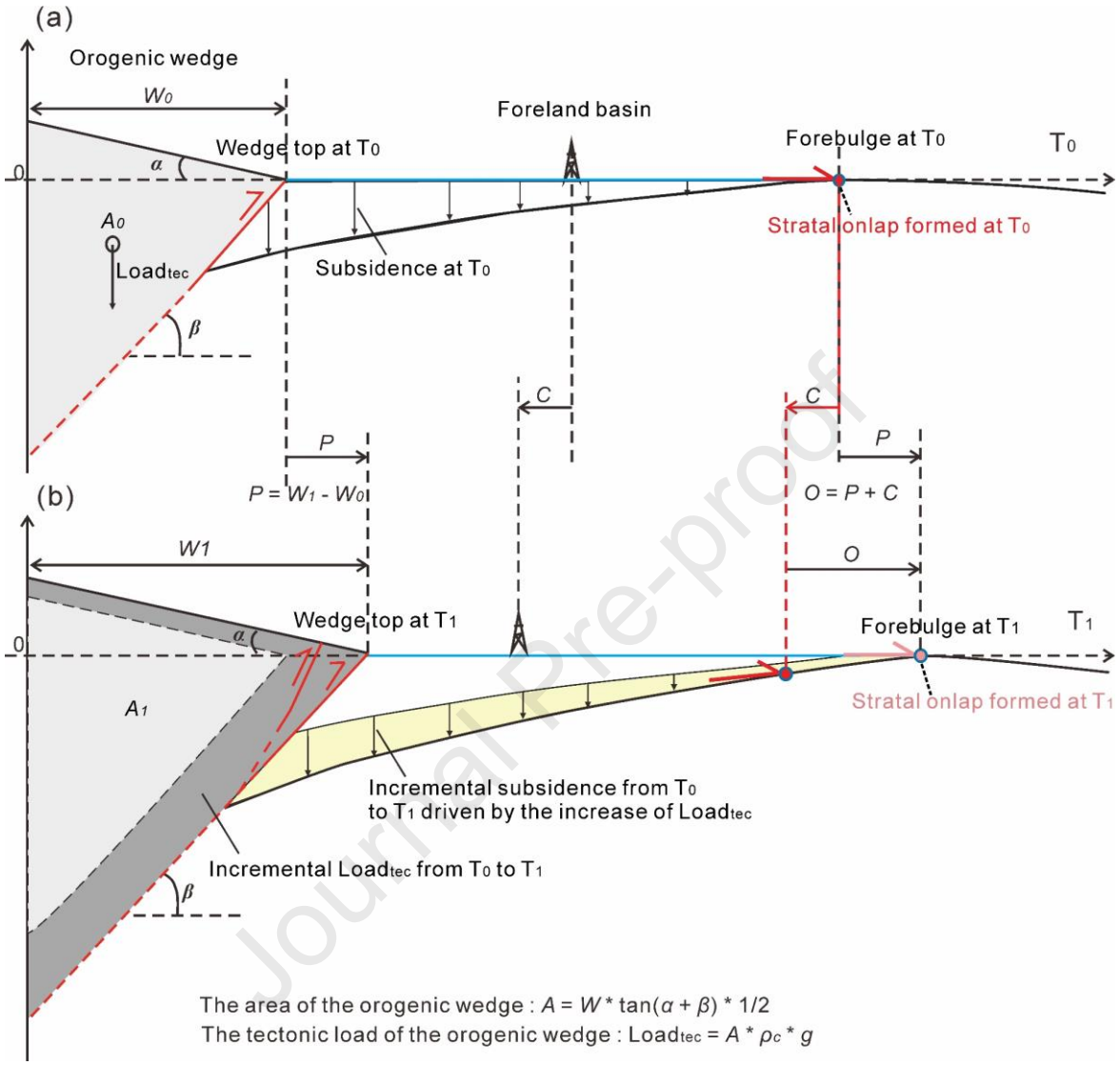

Figure 6 (a) (b) A scheme of the numerical foreland basin model. In a foreland basin-thrust wedge system, the increase of tectonic load (buildup) of the thrust wedge can cause flexure of the underlying plate to form a foreland basin which is the subsidence in the coupled foreland basin (DeCelles & Giles, 1996). Buildup of the thrust wedge also cause migration of the forebulge to the foreland. Furthermore, underthrusting of the underlying plate beneath the orogen lead to migration of the foreland basin to the foreland. Thus, the migration of the foreland basin (*O*), recorded by the stratal onlaps, consists of the propagation of an orogenic wedge (*P*) and the

convergence between the underlying plate and the thrust wedge (*C*) (DeCelles & DeCelles, 2001; Naylor and Sinclair, 2008; DeCelles, 2012), so $O = P + C$. Stratal onlaps in the foreland basin that records its lateral migration (e.g. Li et al., 2019; Wang et al., 2020). This type of onlaps has been identified in the seismic profile of Figs. 7 and S1. The W_0 and W_1 are the widths of the thrust wedge at T_0 and T_1. The V_C, V_P and V_O are the velocity of the *C*, *P* and *O*, respectively.

Figure 7

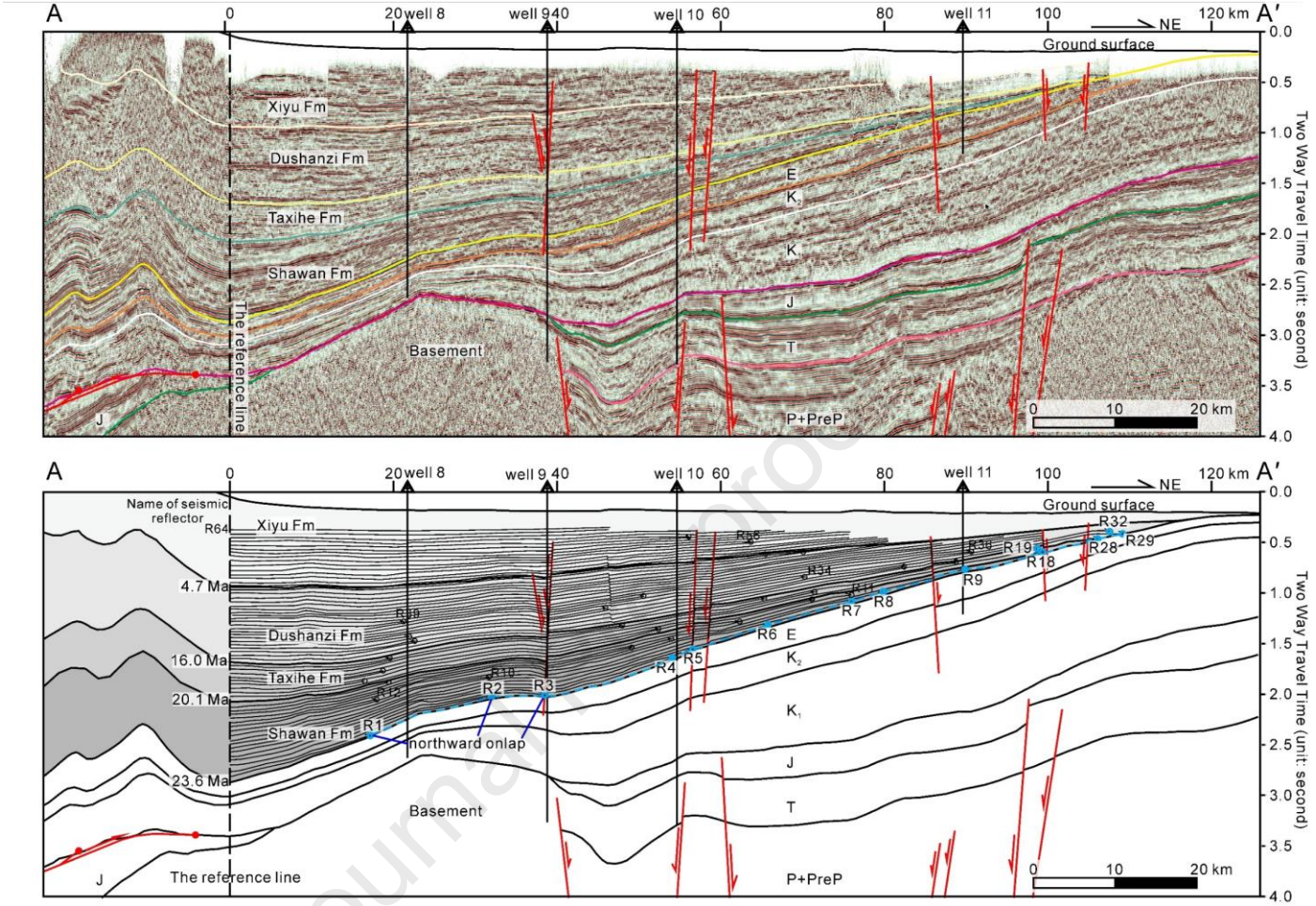

Figure 7 (a) Interpreted seismic profile crossing the foredeep of the SJFB (Wang et al., 2013). See Figure 1b for its location and Figure S1 for its large-scale version. Reflectors are marked with dark blue lines and named R1-R64. (b) Tracing lines of seismic reflectors in the Cenozoic. The arrows indicate reflector terminations. The onlap points toward the foreland are marked with a blue dashed line. The ages of bottoms of the Shawan, Taxihe, Dushanzi, and Xiyu Fms are dated by correlating the seismic reflectors with the magnetostratigraphic studies (Huang et al., 2006; Charreau et al., 2009; Lu et al., 2010). See Wang et al. (2013) for the correlation between the seismic profiles and the magnetostratigraphic results.

Figure 8

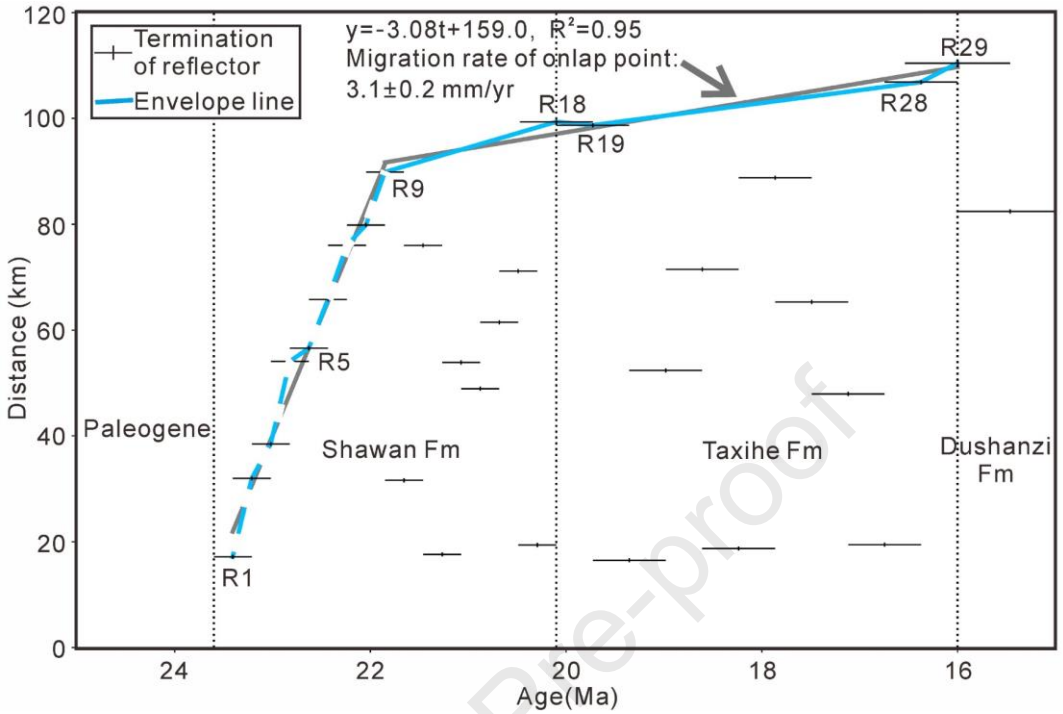

Figure 8 Plot of reflectors ages of the Southern Junggar foreland sequences and distances from their termination points to the northern Tian Shan wedge. Open symbols indicate values measured from the reference line to terminations on Fig. 7. See Table S1 for all the measured values. The blue line is a distribution envelope established by connecting the maximum values within about one million years. The solid line is fitted by values connected by the dashed fold line. The envelope line of terminations indicates migration of the forebulge.

Figure 9

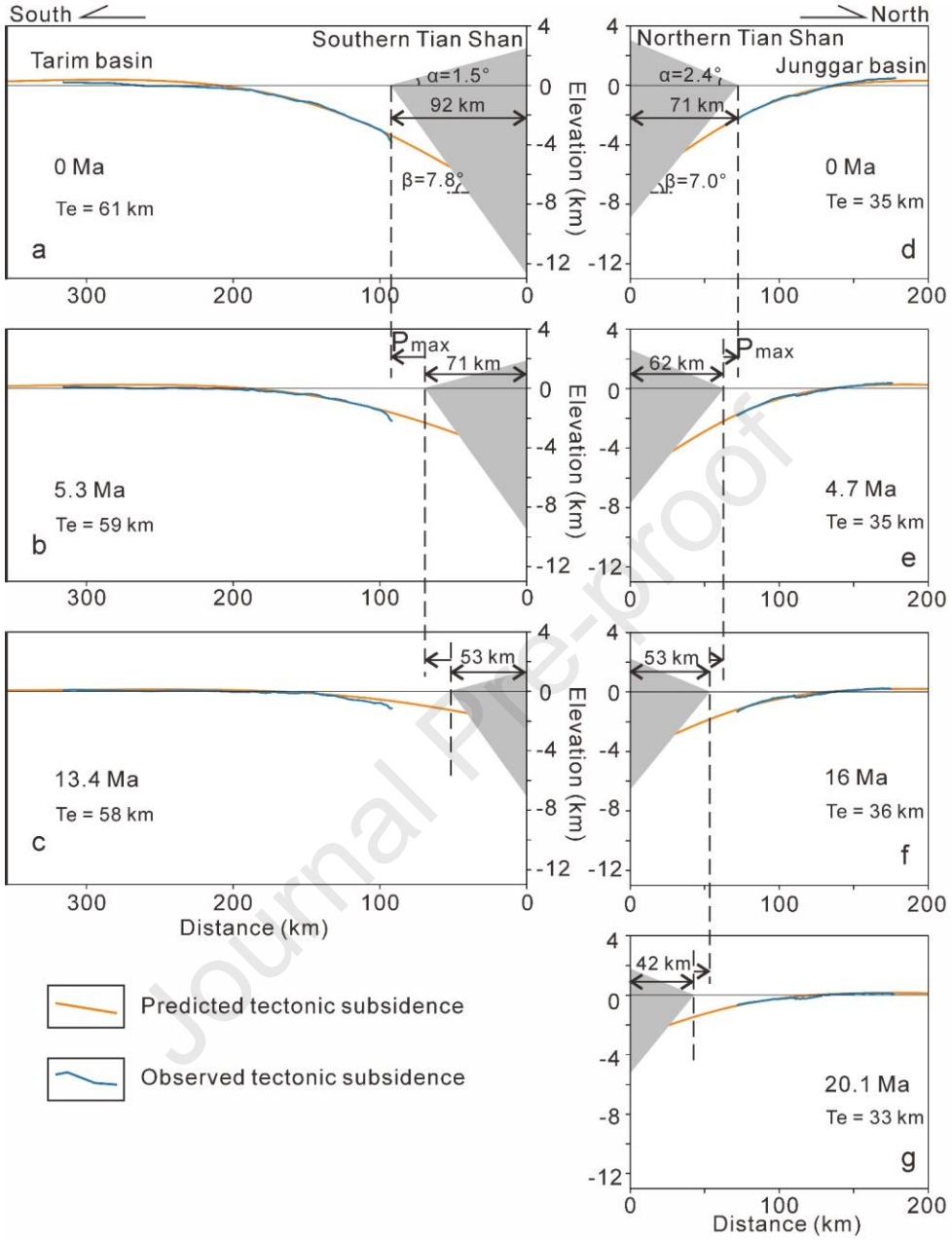

Figure 9 (a), (b) & (c) Modelled tectonic subsidence profiles across the NTFB at three moments from the first end-member model. (d), (e), (f) & (g) Modelled tectonic subsidence profiles across the SJFB at four moments from the first end-member model. The convergence distance (*C* in Fig. 6) between the thrust wedge and the basin basement in the model is set to zero. The grey triangles represent the predicted topographic loads of the southern and northern Tian Shan thrust wedges. The variation of the triangle widths indicates the maximum value of propagation (*P*) of the southern and northern Tian Shan wedges.

Figure 10

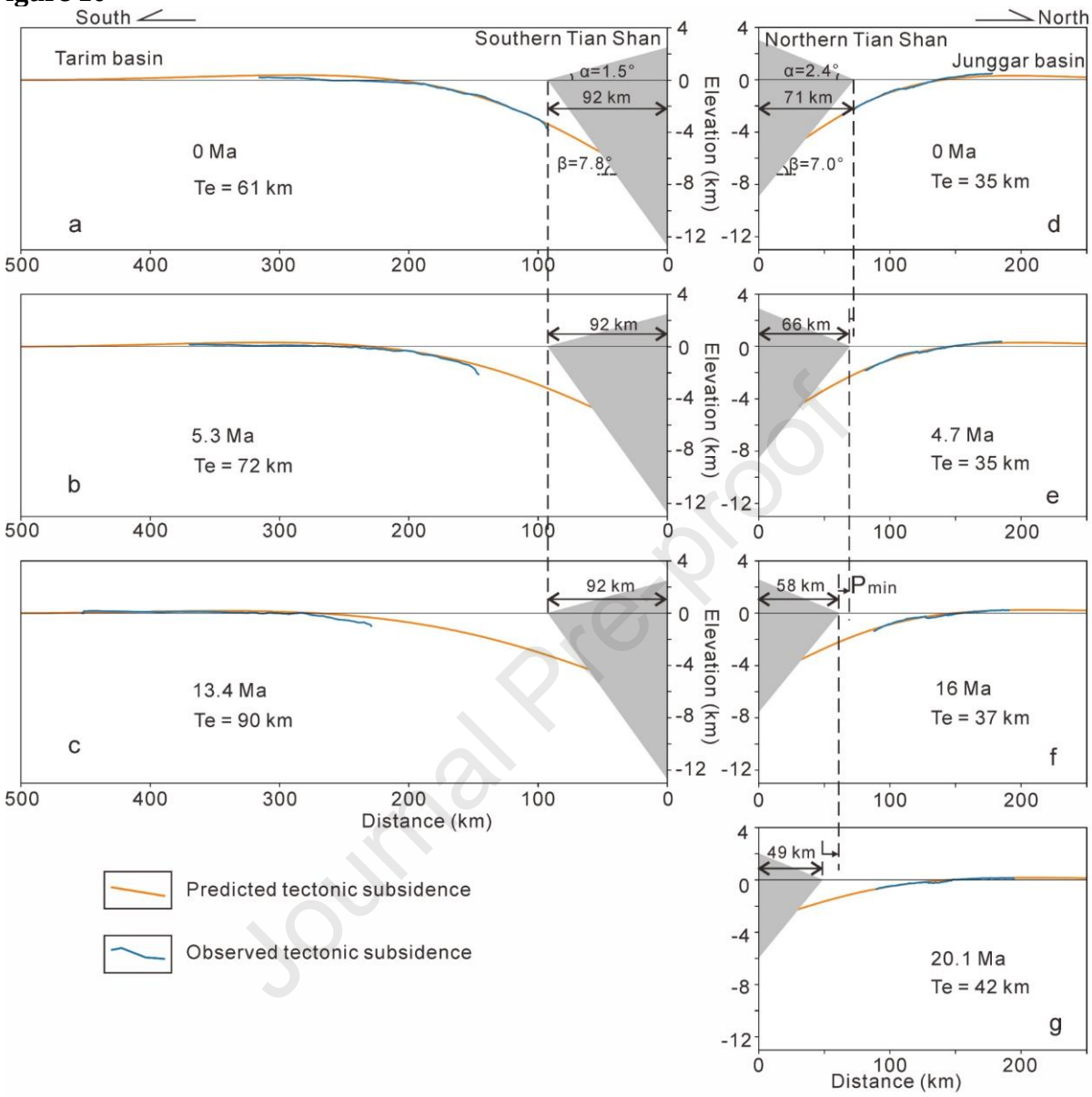

Figure 10 (a), (b) & (c) Modelled tectonic subsidence profiles across the NTFB at three moments from the second end-member model with a theoretical maximum value of the horizontal convergence between the thrust wedge and basin basement equaling to the migration distance of the foreland basins. (d), (e), (f) & (g) Modelled tectonic subsidence profiles across the SJFB at four moments from the second end-member model. The grey triangles represent the predicted topographic loads of the southern and northern Tian Shan thrust wedges. The variation of the triangle widths indicates the minimum value of propagation (*P*) of the southern and northern Tian Shan wedges.

Figure 11

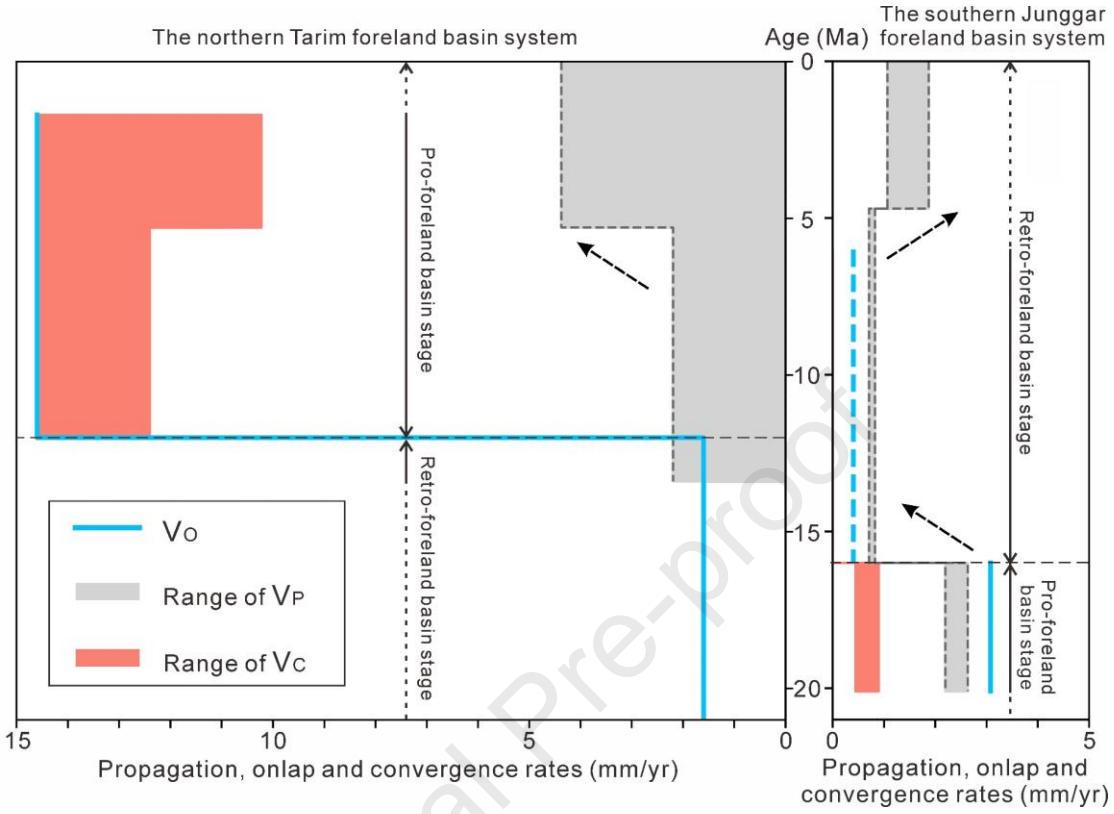

Figure 11 The evolution of the forelandward onlap rate, propagation rate of the thrust wedge and the convergence rate in the NTFB and SJFB systems. The dash blue line in the plot of the SJFB represents the migration rate of the conglomerate-sandstone transition in the foreland sequence to the ~40 km west of profile BB' (Li et al., 2022). The black arrows indicate the changes in the propagation rate of the predicted topographic loads of the southern and northern Tian Shan wedges.

1420 **Figure 12**

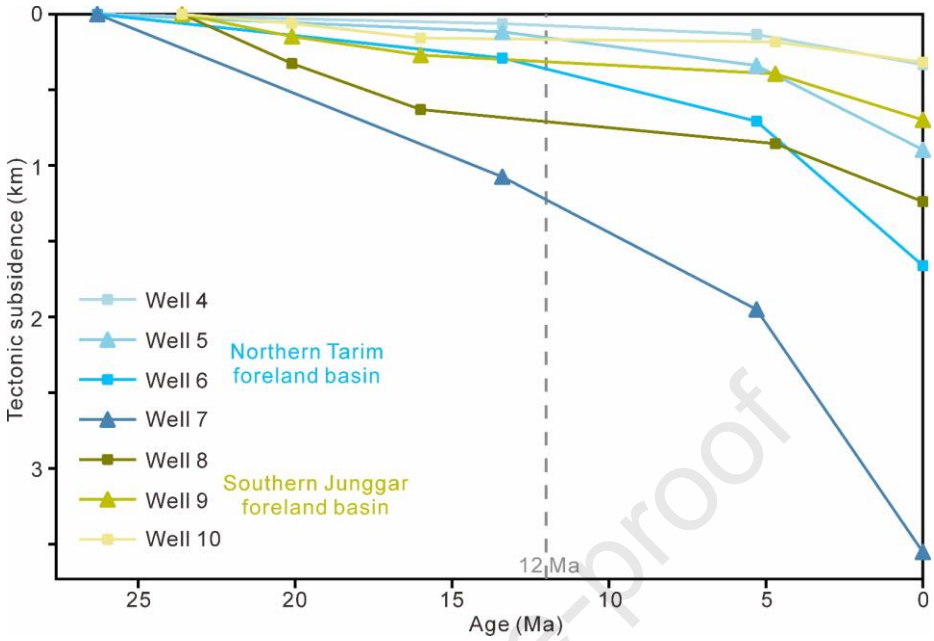

1421

1422 Figure 12 Neogene tectonic subsidence curves of wells 4, 5, 6 and 7 in the NTFB and wells 8, 9 and

1423 10 in the SJFB. Well positions are shown in Figs. 1b and 4. The tectonic subsidence curve is yielded by

1424 flexural back stripping, paleo-bathymetric corrections and eustatic corrections using data from the wells.

1425 The average tectonics subsidence rates of the seven wells are listed in Table 3.

1426

Figure 13

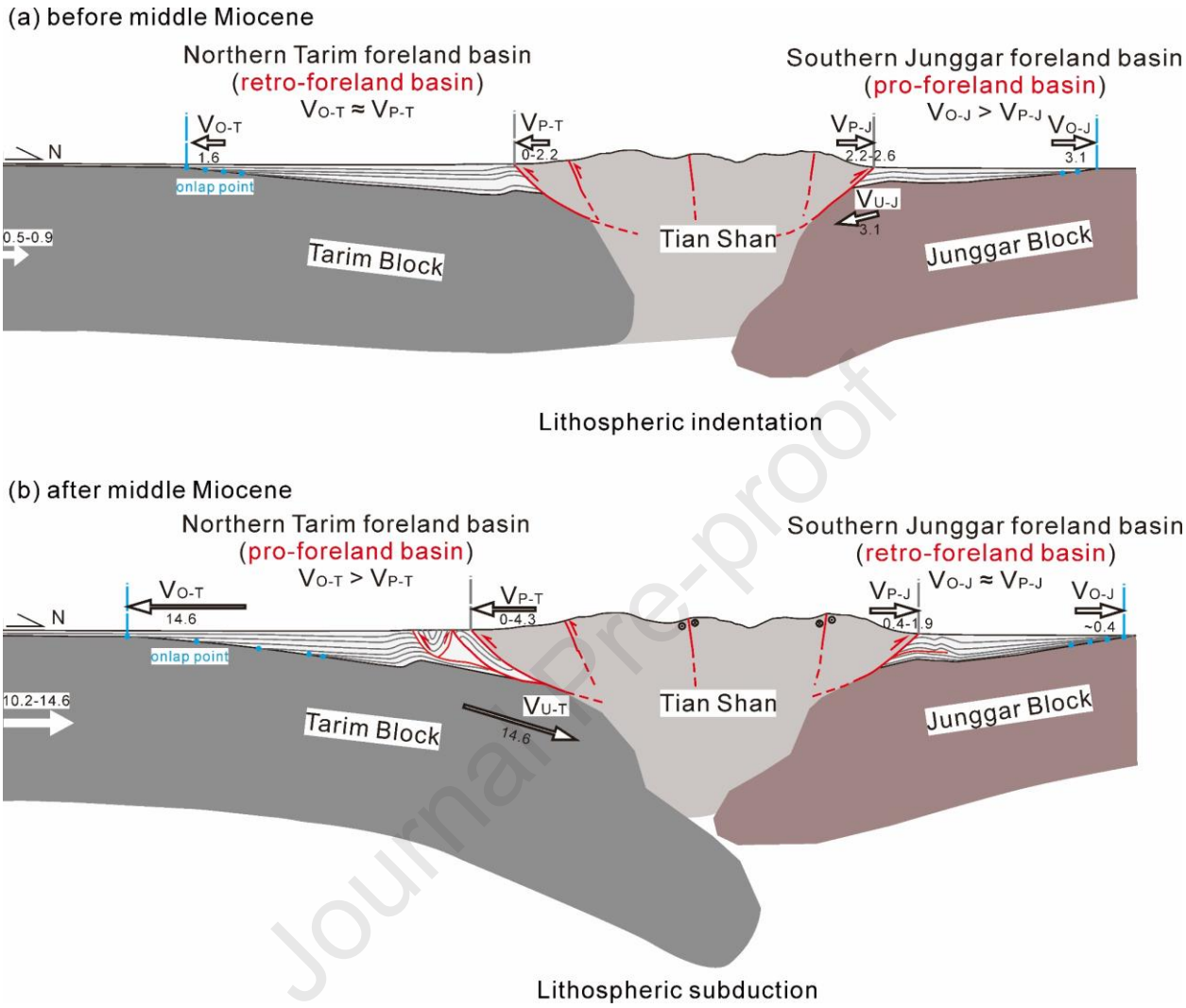

Figure 13 The deep structure of the middle segment of the Tian Shan unraveled by the evolution of the bilateral foreland basins. The length of the arrows represents the relative velocity of the propagation rate of the thrust wedge ($V_{P\text{-}T}$, $V_{P\text{-}J}$), the onlap rate of the foreland sequence ($V_{O\text{-}T}$, $V_{O\text{-}J}$) and the underthrusting rate ($V_{U\text{-}T}$, $V_{U\text{-}J}$) in the NTFB and SJFB.

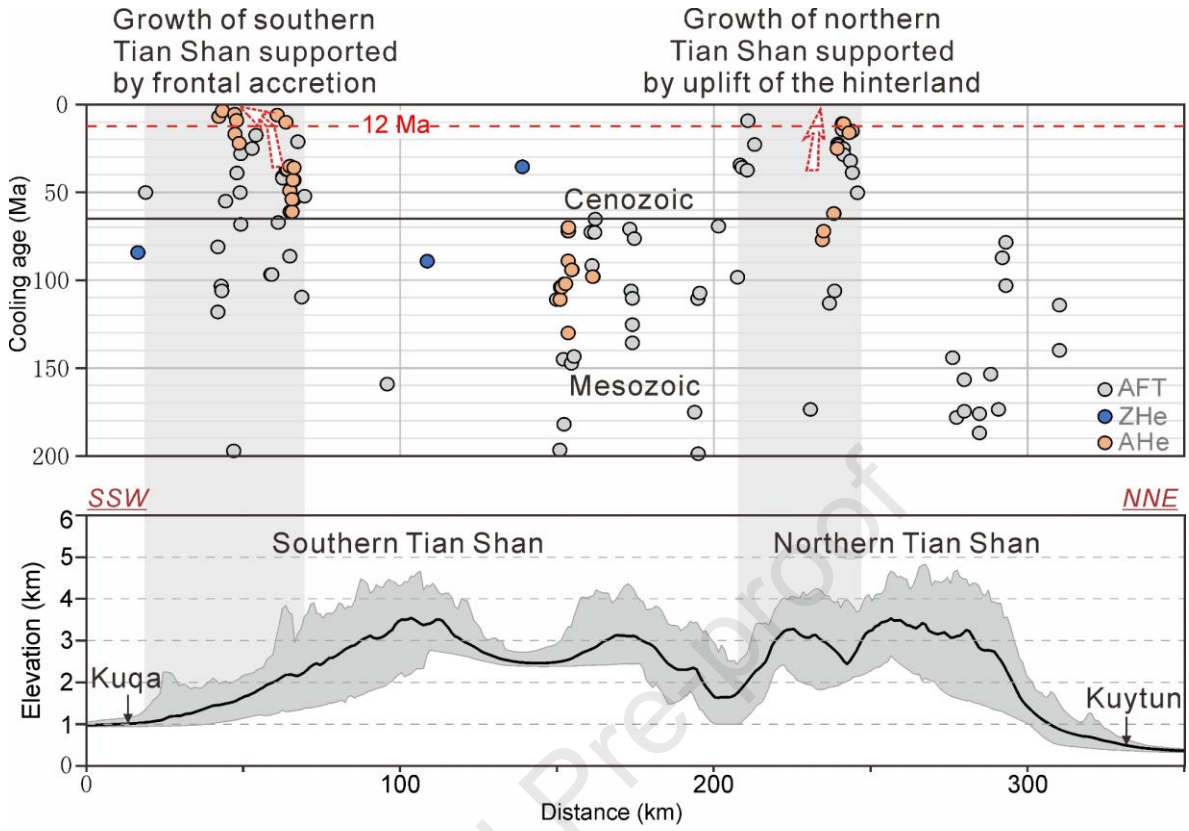

Figure 14 The Cenozoic cooling ages obtained around and in the same swath profile across the middle segment of the Tian Shan, location is referred in Figure 1b (data sources: Dumitru et al., 2001; Yang et al., 2003; Zhang et al., 2007; Du et al., 2007; Wang et al., 2008; 2009; Jolivet et al., 2010; Chang et al., 2017a). The dashed arrows show the incoming flux in the pro-side and retro-side. Table of individual ages and their associated metadata can be found in Tables S3 in the Supplementary material. AFT - apatite fission-track, ZHe - zircon (U-Th)/He and AHe - apatite (U-Th)/He.

Table 1

Table 1 Lithological and decompaction parameters used in back stripping (Sclater and Christie, 1980).

Lithology	Compaction decay length D^* (10^5/cm^{-1})	Initial porosity ϕ_0	Sediment grain density ρ_S (g cm^{-3})
Sandstone	0.27	0.49	2.65
Shale	0.51	0.63	0.72
Shaly sand	0.39	0.56	2.68

Table 2

Table 2 The onlap rates of the foreland sequence, propagation rate of the thrust wedge and the crustal shortening rate in the Northern Tarim and southern Junggar foreland basin systems. The stratal onlap rates are determined by the interpretations of the seismic profiles across the NTFB (Li et al., 2019) and SJFB.

Northern Tarim foreland basin-thrust wedge system					
Time (Ma)	Propagation rate of thrust wedge (mm/yr)	Time (Ma)	Stratal onlap rate (mm/yr)	Time (Ma)	Convergence rate (mm/yr)
0–5.3	0–4.4	1.7–12.0	14.6	1.7–5.3	10.2–14.6
5.3–13.4	0–2.2	12.0–26.0	1.6	5.3–12.0	12.4–14.6
				12.0–13.4	0–1.6
Southern Junggar foreland basin-thrust wedge system					
Time (Ma)	Propagation rate of thrust wedge (mm/yr)	Time (Ma)	Stratal onlap rate (mm/yr)	Time (Ma)	Convergence rate (mm/yr)
0–4.7	1.1–1.9				
4.7–16.0	0.7–0.8	4.7–16.0	0.4*	4.7–16.0	0
16.0–20.1	2.2–2.6	16–20.1	3.08	16.0–20.1	0.5–0.9

*This is the forelandward migration rate of the conglomerate-sandstone transition in the foreland sequence of the SJFB, which reveals the onlap rate of the foreland sequences (Li et al., 2022).

Table 3

Table 3 The tectonic subsidence rates of Wells 4, 5, 6 & 7 in the NTFB and Wells 8, 9 & 10 in the SJFB from back stripping. Well positions are shown in Figs. 1b and 4.

Northern Tarim foreland basin				
Time (Ma)	Tectonic subsidence rate (mm/yr)			
	Well 4	Well 5	Well 6	Well 7
0–5.3	37.5	104.9	180.0	302.5
5.3–13.4	8.9	27.5	51.6	108.1
13.4–26.3	4.8	9.0	11.0	40.8
Southern Junggar foreland basin				
Time (Ma)	Tectonic subsidence rate (mm/yr)			
	Well 8	Well 9	Well 10	
0–4.7	81.5	64.7	28.5	
4.7–16.0	17.8	11.0	2.3	
16.0–20.1	80	28.8	21.0	
20.1–23.6	93.1	43.4	20.1	

Highlights:

- The forebulge of the southern Junggar foreland basin (SJFB) migrated northward at ~3.1 mm/yr during ~22–16 Ma.
- The northern Tarim foreland basin was a retro-foreland basin, while SJFB was a pro-foreland basin before the middle Miocene, but they converted later.
- The Tarim block was an overriding plate before the middle Miocene, while the Junggar block was an underthrusting plate, but they switched roles after the middle Miocene.

Declaration of interests

☐ The authors declare that they have no known competing financial interests or personal relationships that could have appeared to influence the work reported in this paper.

☒ The authors declare the following financial interests/personal relationships which may be considered as potential competing interests:

Chao LI reports financial support was provided by The National Natural Science Foundation of China.